nature chemistry

SUPPLEMENTARY INFORMATION

https://doi.org/10.1038/s41557-019-0288-8

In the format provided by the authors and unedited.

Super-resolution imaging of non-fluorescent reactions via competition

Xianwen Mao[1], Chunming Liu[1], Mahdi Hesari[1], Ningmu Zou[1,2] and Peng Chen[1]*

[1]Department of Chemistry and Chemical Biology, Cornell University, Ithaca, NY, USA. [2]Present address: AMD Inc., Austin, TX, USA.
*e-mail: pc252@cornell.edu

Supplementary Information for

Super-resolution imaging of nonfluorescent reactions via competition

Xianwen Mao, Chunming Liu, Mahdi Hesari, Ningmu Zou, and Peng Chen*

*Correspondence to: pc252@cornell.edu

Contents

1. Materials and methods

1.1. Synthesis of $BiVO_4$ particles

$BiVO_4$ particles with a tetragonal bifrustum morphology were synthesized by a hydrothermal procedure using a modified method reported by Li *et al*.[1] and characterized by scanning electron microscopy (SEM). Typically, 3 mmol NH_4VO_3 (Sigma-Aldrich, 398128-50G) and 3 mmol $Bi(NO_3)_3 \cdot 5H_2O$ (Sigma-Aldrich, 383074-100G) were dissolved in 30 mL of 1 M nitric acid solution (Sigma-Aldrich, 438073-500ML), and the pH of the resulting solution was adjusted to about 1 with ammonia solution (EMD Millipore, 1054232500). Next, the solution was hydrothermally treated in a 100 mL borosilicate glass bottle (Fisherbrand) inside a furnace (Thermo Scientific Lindberg/Blue M) at 80 °C for 48 h, and the yellow solid powder was then separated by filtration, followed by washing with water for several times and drying in air at 60 °C for 24 h. Representative SEM images (Supplementary Figure 1) of the as-synthesized $BiVO_4$ particles show that the majority of them exhibit the tetragonal bifrustum morphology with exposed {010} basal facets and {110} lateral facets.

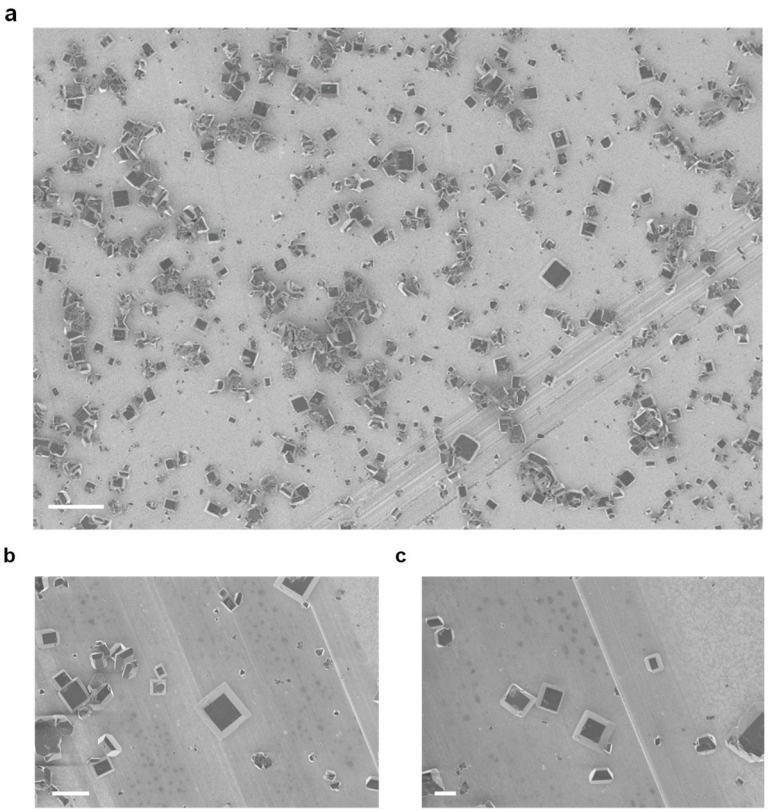

Supplementary Figure 1. Representative SEM images of $BiVO_4$ particles synthesized in this study. Scale bars in panels **a**, **b**, and **c** are 20, 5, and 2 μm, respectively.

1.2. Ensemble photoelectrocatalytic measurements

Ensemble-level photoelectrochemical measurements were performed with a potentiostat (CH Instrument, CHI1200a) in a three-electrode configuration using $BiVO_4$-modifed ITO electrodes (prepared by drop-cast 0.5 mL of 10 mg/mL $BiVO_4$ suspensions onto an ITO-coated slide (Delta Technologies, CB-50IN-0105) followed by annealing at 450 °C for 1 h) as the working electrode, a Pt wire (BASi, MW-1033) as the counter electrode, and a Ag/AgCl electrode (BASi, MF-2052) as the reference electrode. A quartz cell of 1 cm × 4 cm × 4 cm (Starna Cells, 1-Q-40) was employed as the working electrode chamber, which

can be illuminated by an expanded 405 nm laser beam with a radius of 1.2 cm and a power density of 5.3 × 10^{-3} W cm^{-2}. The working electrode chamber was kept under N_2 atmosphere, and separated from the counter electrode chamber by a salt bridge. The electrolyte solution was deaerated 0.1 M Na_2SO_4, 0.1 M pH 7.4 phosphate buffer. Similar to the AR oxidation reaction rate (Eq. 1 in the main text), the HQ oxidation reaction rate follows the saturation kinetics with competitive inhibition by AR[2]:

$$v_{HQ} = \frac{k_{HQ} K_{HQ} [HQ]}{1 + K_{AR}[AR] + K_{HQ}[HQ]} \qquad \text{Eq. S1}$$

where v_{HQ} and k_{HQ} are the (specific) rate and (specific) rate constant of the HQ oxidation reaction, K_{AR} and K_{HQ} are the adsorption equilibrium constants for AR and HQ on the catalyst surface, respectively, as discussed below. In the absence of the competing AR molecule, Eq. S1 reduces to the classic Langmuir saturation kinetics; and at the low [HQ] limit, $v_{HQ} = k_{HQ}K_{HQ}[HQ]$, and at the limit of saturating [HQ], $v_{HQ} = k_{HQ}$.

The complete reaction scheme for the competition between the AR oxidation reaction and the HQ oxidation reaction is shown below, each following effective Langmuir adsorption mechanism followed by catalytic conversion to the product on the surface the catalyst:

$$\text{SS + AR} \underset{k_{-1}}{\overset{k_1}{\rightleftharpoons}} \text{SS-AR} \xrightarrow{k_2} \text{SS + Rf}$$

$$\text{SS + HQ} \underset{k_{-3}}{\overset{k_3}{\rightleftharpoons}} \text{SS-HQ} \xrightarrow{k_4} \text{SS + Q}$$

where SS represents a surface site on the catalyst particle, SS-AR and SS-HQ indicate surface-bound AR and HQ, respectively, and Rf and Q denotes resorufin and quinone, the product molecules from AR and HQ oxidation reactions, respectively, and k_i (i = 1, −1, 2, 3, −3, 4) are the associated rate constants. Based on the reaction scheme above that shows the competition between AR and HQ oxidation reactions, $K_{AR} = \frac{k_1}{k_{-1} + k_2}$ and $K_{HQ} = \frac{k_3}{k_{-3} + k_4}$ in Eq. S1 [2]. Under the condition of fast adsorption-desorption equilibrium of the reactants (i.e., Langmuir adsorption equilibrium is maintained during catalysis) $k_2 \ll k_{-1}$, $k_4 \ll k_{-3}$, and consequently, $K_{AR} = \frac{k_1}{k_{-1}}$ and $K_{HQ} = \frac{k_3}{k_{-3}}$. Therefore, K_{AR} and K_{HQ} represent the adsorption equilibrium constants for AR and HQ on the catalyst surface, respectively.

Global fitting of the ensemble kinetics data (i.e., AR and HQ oxidation rates versus [HQ], Fig. 1d in the main text) with Eq. 1 and Eq. S1 yielded k_{AR} = (1.73 ± 0.16) × 10^{-3} μM s^{-1}, K_{AR} = (1.56 ± 0.14) × 10^{-1} μM^{-1}, k_{HQ} = (2.27 ± 0.12) × 10^{-2} μM s^{-1}, and K_{HQ} = (3.24 ± 0.38) × 10^{-2} μM^{-1} (error bars: s.d.).

Notably, based on the main text Eq.1 (i.e., $v_{AR} = \frac{k_{AR} K_{AR} [AR]}{1 + K_{AR}[AR] + K_{HQ}[HQ]}$), it can be seen that in the HQ titration experiments with a fixed AR concentration, v_{AR}^{-1} scales linearly with [HQ] (see Eq. S2 below), with the scaling constant being $\frac{K_{HQ}}{k_{AR} K_{AR} [AR]}$, which is directly proportional to K_{HQ}.

$$v_{AR}^{-1} = \frac{1 + K_{AR}[AR] + K_{HQ}[HQ]}{k_{AR} K_{AR} [AR]} = \frac{1}{k_{AR} K_{AR} [AR]} K_{HQ}[HQ] + \frac{1 + K_{AR}[AR]}{k_{AR} K_{AR} [AR]} \qquad \text{Eq. S2}$$

As a result, at any fixed [AR], the difference in v_{AR}^{-1}, $\Delta(v_{AR}^{-1})$, between a condition in the presence of HQ (e.g., [HQ] = 100 μM) and the condition in the absence of HQ (i.e., [HQ] = 0 μM) is directly proportional to K_{HQ}, as shown in the equation below:

$$\Delta\left(v_{AR}^{-1}\right) = \left(v_{AR}^{-1}\right)_{[HQ]\neq 0} - \left(v_{AR}^{-1}\right)_{[HQ]=0} = \frac{[HQ]}{k_{AR}K_{AR}[AR]}K_{HQ} \qquad \text{Eq. S3}$$

The number of product molecules (n_p) generated from the AR oxidation reaction within a given catalyst surface area (e.g., the bin size in the two-dimensional histogram, see Fig. 2 a – c in the main text) over a given period of time scales linearly with v_{AR}, based on the relation that $n_p = v_{AR}t_{movie}A_{bin}$, where t_{movie} is the duration of the movie, and A_{bin} is the bin size of the image plot (e.g., Fig. 2a). Therefore, n_p^{-1} also scales linearly with [HQ], with the scaling constant being proportional to K_{HQ}. Therefore, the difference, $\Delta(n_p^{-1})$, between n_p^{-1} obtained with a given HQ concentration (e.g., [HQ] = 100 μM) and n_p^{-1} obtained with [HQ] = 0 μM is directly proportional to K_{HQ}, as shown in the equation below.

$$\Delta\left(n_p^{-1}\right) = \frac{1}{t_{movie}A_{bin}} \times \frac{[HQ]}{k_{AR}K_{AR}[AR]}K_{HQ} \propto K_{HQ} \qquad \text{Eq. S4}$$

1.3. COMPEITS imaging experiments

A schematic illustration of the COMPEITS imaging experimental setup is shown in Supplementary Figure 2 (similar to Fig. 1a in the main text), which is based on single-molecule fluorescence microscopy[3-9] with two-laser epifluorescence illumination on an inverted OLYMPUS IX71 microscope. $BiVO_4$ particles were spin-coated onto an ITO electrode and annealed at 450 °C for 1 h, and then assembled into a three-electrode photoelectrochemical microfluidic cell (about 5 mm wide and 100 μm high) using double-sided tape sandwiched between an ITO electrode and a coverslip. The reactant solution (deaerated 0.1 M Na_2SO_4, 0.1 M pH 7.4 phosphate buffer with appropriate quantities of AR and HQ) was continuously supplied to the photoelectrochemical cell at a volumetric flow rate of 25 μL min^{-1}. The ITO electrode with dispersed $BiVO_4$ particles serves as the working electrode, the potential of which was controlled to be at 0.2 V via a potentiostat (CH Instrument, CHI1200a), and a platinum wire (BASi, MW-4139) and a Ag/AgCl electrode (BASi, MW-2030) were used as the counter and reference electrode, respectively. A continuous wave circularly polarized 405-nm laser (COHERENT, OBIS 405LX) excites the $BiVO_4$ particles to generate charge carriers while a 532-nm laser (COHERENT, SAPPHIRE 532-50CW CDRH) induces the fluorescence of the reaction product resorufin. The two lasers were combined via a 425 nm long-pass dichroic mirror (THORLAB, DMLP425), focused onto the back aperture of a 60x water immersion objective (OLYMPUS, UPLSAPO60XW), and reflected by a 550 nm long-pass dichroic mirror (CHROMA, E550LP) to illuminate the sample in an epi-illumination geometry over an 70 × 60 μm^2 area. The fluorescence was collected through the same 60x objective, passed through the 550 nm long-pass dichroic mirror and a 580 ± 30 nm emission filter (CHROMA, HQ580/60m), and imaged by an electron multiplying charge coupled device (EMCCD) camera (ANDOR, DU-897E-CS0-#BV) operated at a 15-ms frame rate, which is controlled by the ANDOR IQ3 software.

In a typical experiment, 1000 fluorescence images in the absence of the fluorogenic reactant (i.e., AR) were collected first (in order to obtain the steady photoluminescence intensities of $BiVO_4$ particles, see Section 1.4.1), followed by collecting another 30000 fluorescence images with appropriate quantities of AR and HQ. The detailed analysis procedure of the fluorescence images obtained is described in Section 1.4.

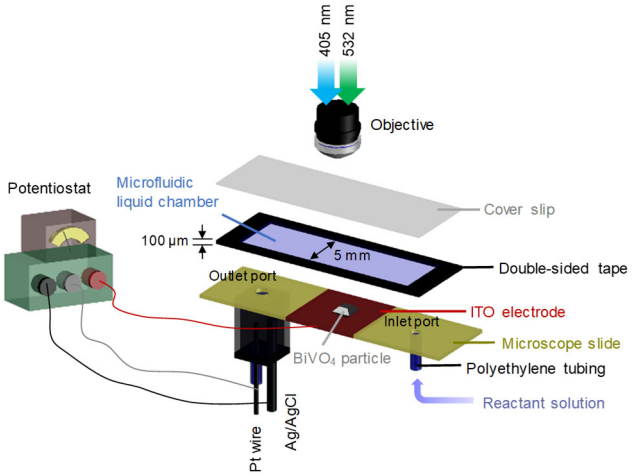

Supplementary Figure 2. Schematic illustration of the COMPEITS imaging experimental setup. A three-electrode photoelectrochemical microfluidic cell (5 mm wide and 100 µm high) was assembled using double-sided tape sandwiched between an ITO electrode coated with dispersed $BiVO_4$ particles and a coverslip. The potential of the ITO electrode was controlled by a potentiostat and the microfluidic liquid cell was subject to 405-nm/532-nm two-laser wide-field epi-illumination via the objective. The reactant solution was driven by a syringe pump to the liquid chamber continuously with a controlled volumetric flow rate through a polyethylene tubing.

In a typical COMPEITS measurement, AR titration experiments (Supplementary Figure 3) in the absence of HQ ([AR]: 2 to 100 µM; 405-nm laser power density: 3.1×10^{-2} W cm^{-2}; 532-nm laser power density: 1.8×10^{2} W cm^{-2}) were performed first to determine the adsorption equilibrium constant for AR (K_{AR}) using:

$$v_{AR} = \frac{k_{AR} K_{AR} [AR]}{1 + K_{AR} [AR]} \qquad \text{Eq. S5}$$

where v_{AR} and k_{AR} are the specific rate and specific rate constant of the AR oxidation reaction. Next, HQ titration experiments in the presence of AR (Supplementary Figure 15) ([AR]: 50 nM; [HQ]: 0 – 2 mM; 405-nm laser power density: 1.2×10^{2} W cm^{-2}; 532-nm laser power density: 1.8×10^{2} W cm^{-2}) were carried out with the same set of $BiVO_4$ particles as those in the AR titration experiments to determine the adsorption equilibrium constants for HQ (i.e., K_{HQ}) via Eq. 1 by using the pre-quantified K_{AR} (i.e., the HQ titration data were fitted with Eq. 1 using two floating parameters, k_{AR} and K_{HQ}, and a fixed value for K_{AR}). In most cases, the fitting was performed using v_{AR} *versus* [HQ] plots instead of v_{AR}^{-1} *versus* [HQ] plots.

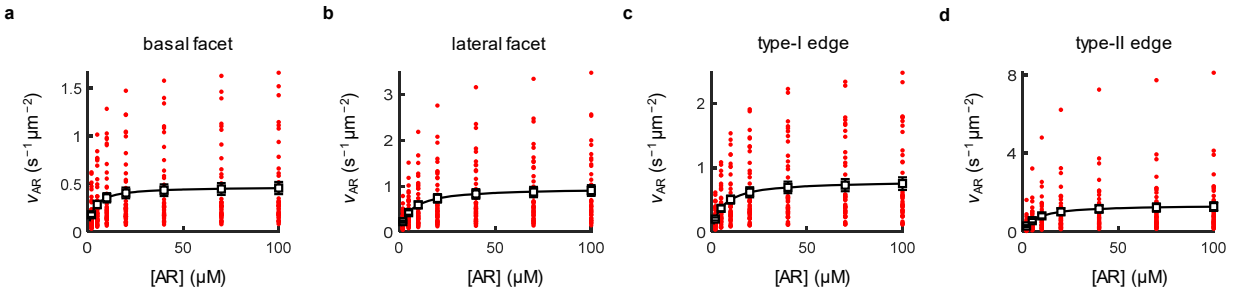

Supplementary Figure 3 AR titration experiments in the absence of HQ to determine K_{AR}. The dependence of the specific AR reaction rate v_{AR} on the AR concentration for the basal {010} facet (**a**), lateral {110} facet (**b**), type-I edge (**c**), and type-II edge (**d**). dots: data from the 42 particles investigated in this study. Black squares: data averaged over the 42 particles. Error bars: s.e.m. Solid lines: fits with Eq. S2. For the basal {010} facet, $k_{AR} = (4.69 \pm 0.03) \times 10^{-1}$ s^{-1} µm^{-2} and $K_{AR} = (3.07 \pm 0.09) \times 10^{-1}$ µM^{-1};

for the lateral {110} facet, k_{AR} = (9.58 ± 0.11) × 10^{-1} s^{-1} μm^{-2} and K_{AR} = (1.58 ± 0.08) × 10^{-1} μM^{-1}; for the type-I edge, k_{AR} = (7.93 ± 0.07) × 10^{-1} s^{-1} μm^{-2} and K_{AR} = (1.71 ± 0.06) × 10^{-1} μM^{-1}; for the type-II edge, k_{AR} = 1.37 ± 0.02 s^{-1} μm^{-2} and K_{AR} = (1.43 ± 0.07) × 10^{-1} μM^{-1}. Error bars for the fitted values are s.d. These K_{AR} values are in accordance with that obtained from ensemble experiments (i.e., within the same order of magnitude; see Supplementary Note 1.2).

Under our COMPEITS imaging experimental conditions, the catalytic activities of $BiVO_4$ particles were stable over the entire course of measurements (~ 2 weeks) (Supplementary Figure 4). The assembled flow cells usually can last for 2 to 3 weeks if the solvent is water, without observing contamination by impurities possibly from double-sided tapes. However, it should be noted that if an organic solvent (e.g., hexane) was used in the flow cell, impurities may leach out from double-sided tapes and thus might cause some background issues even within a few hours of imaging experiments. The sequence of the HQ titration experiments was from a reaction condition with no HQ to reaction conditions with increasingly higher HQ concentrations (50, 100, 250, 500, 1000, 2000 µM). Two tests were performed by flowing in the reactant solution without HQ (i.e., with only [AR] = 50 nM) after imaging experiments with [HQ] = 250 and 2000 µM; both cases showed similar activities to those obtained with the initial run without HQ.

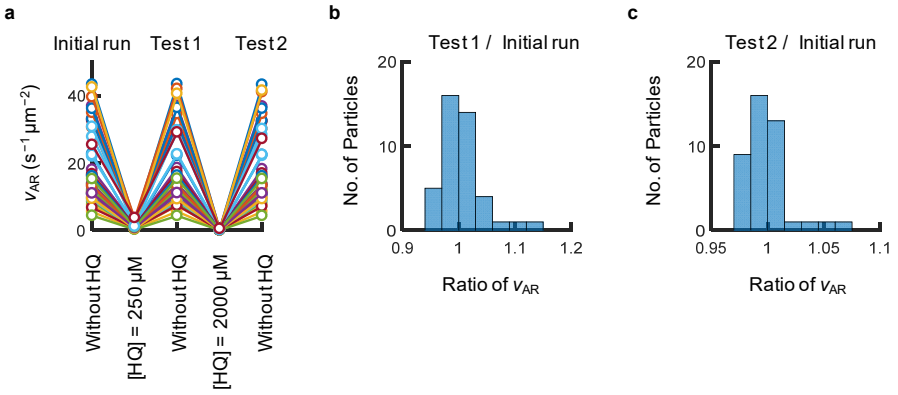

Supplementary Figure 4. Catalytic activities of $BiVO_4$ particles were stable over the entire course of measurements under our COMPEITS imaging experimental conditions. **a**, Comparison of specific AR reaction rate of the whole particle, v_{AR}, for the initial run without HQ, the COMPEITS run with [HQ] = 250 µM, test 1 without HQ, the COMPEITS run with [HQ] = 2000 µM, and test 2 without HQ. The same particle was labeled with the same color. The measurements were performed in the following chronological order: initial run without HQ, COMPEITS runs with [HQ] = 50, 100 and 250 µM, test 1 without HQ (about 1 week after the initial run), COMPEITS runs with [HQ] = 1000 and 2000 µM, and test 2 without HQ (about 2 weeks after the initial run). **b-c**, Histograms of the ratios of v_{AR} between test 1 and the initial run (**b**), and between test 2 and the initial run (**c**), showing that the catalytic activities of the $BiVO_4$ particles were stable over the course of imaging measurements.

1.4. Analysis procedure of COMPEITS imaging results

1.4.1. *Analysis of fluorescence images*

The fluorescence images were analyzed using a home-written MATLAB program, iQPALM (image-based quantitative photo-activated localization microscopy), the details of which have been reported in our previous study [10]. For the current work, a few modifications were made and are detailed in this section.

The microscope stage drift was monitored in a frame-by-frame fashion by calculating the intensity-weighted centroid position ($\mu_{IW,x}$, $\mu_{IW,y}$) of the stable intrinsic photoluminescence of the $BiVO_4$ crystals (Supplementary Figure 5a). The average drift of multiple particles present in the same movie (e.g., particles 1, 2 and 3 in Supplementary Figure 5a) was used to correct the centroid position of each candidate fluorescent product molecule. The error in our drift correction method is ~2 nm, as estimated by the

standard deviation of the distributions of drift-corrected $\mu_{IW,x}$ and $\mu_{IW,y}$ (Supplementary Figure 5 b and c). Because the $BiVO_4$ crystals are constantly bright objects, prior to detection of single-molecule fluorescence signals, the average photoluminescence of the $BiVO_4$ crystals was subtracted. 1000 frames in the absence of the fluorogenic reactant AR (i.e., without producing any fluorescent product molecules) were recorded and averaged to generate the average photoluminescence image. Each frame in the catalysis experiment in the presence of AR was subtracted by the stage-drift-corrected, averaged photoluminescence image. After the subtraction of the $BiVO_4$ photoluminescence, the pixels with an intensity value larger than the mean pixel intensity plus six standard deviations were identified as *potential* single molecule fluorescence signals. Specifically, in order to select the candidate pixels, each image after the subtraction of the $BiVO_4$ photoluminescence (Supplementary Figure 6b) was first convoluted with a low-pass Gaussian kernel to produce a slightly smoothed image (Supplementary Figure 6c) with unreasonably small bright spots removed. Then, a boxcar kernel was applied to this smoothed image to generate a spatially non-uniform image background (Supplementary Figure 6d). Subtracting this image background from the original non-smoothed image yielded the final image (Supplementary Figure 6e) that was used for selecting the candidate pixels.

Next, a 13×13 pixel^2 area (each pixel is ~267 nm) centered at each selected pixel was fitted with a two-dimensional Gaussian point spread function (PSF) (Supplementary Figure 6f) to determine the centroid position (x_0, y_0) of each fluorescent product molecule. Such fitting also yields the standard deviation (σ_x, σ_y) and the integrated intensity of the PSF, as well as the localization error (Err_x, Err_y) of the centroid position. Specifically, the two-dimensional Gaussian PSF is of the following form:

$$I(x,y) = C_1 \exp\left(-\frac{(x-x_0)^2}{2\sigma_x^2} - \frac{(y-y_0)^2}{2\sigma_y^2} \right) + C_2 \qquad \text{Eq. S6}$$

where $I(x, y)$ is the EMCCD fluorescence intensity counts, x_0, y_0 are the centroid position of the PSF, σ_x, σ_y are the standard deviations of the Gaussian PSF, and C_1, C_2 are the amplitude and background of the PSF, respectively. The total EMCCD counts (*cts*) of the fitted spots (i.e., the volume of the Gaussian function term Eq. S3) is converted to the total number of fluorescence photons (N) by

$$N = \frac{\left(\frac{cts}{g}\right) \times \left(\frac{S}{QE}\right) \times 3.65}{E_{hv}} \qquad \text{Eq. S7}$$

where g, S, and QE are the EM gain (unitless), sensitivity (electrons per count), and quantum yield (unitless) of the EMCCD camera in the spectral range of detected fluorescence signals, respectively, and E_{hv} (eV) is the energy (2.12 eV) of a single detected fluorescence photon from the product molecule resorufin with an emission maximum wavelength at 585 nm. The numeric value, 3.65, is a physical constant that denotes electron creation in silicon and has a unit of eV per electron. The localization error (Err_x, Err_y) of the centroid position was calculated as

$$Err_i = \sqrt{\frac{\sigma_i^2}{N} + \frac{a^2}{12N} + \frac{8\pi\sigma_i^2 b^2}{a^2 N^2}} \qquad \text{Eq. S8}$$

where a is the pixel size and b is the standard deviation of the spatially non-uniform image background as described earlier. The full details of this fitting routine have been reported in our earlier studies[10,11].

To remove noise contributions and spurious detections, and correct for unresolved multiple-molecule detections and over-counting due to a product molecule adsorbed on the photocatalyst for multiple frames, the selected and PSF-fitted candidate events (i.e., potential single-molecule fluorescence signals) were filtered by a quantitative single-molecule counting algorithm, the details of which can be found in our previous study[11]. Briefly, first, candidate events with their PSF σ_x or $\sigma_y < 100$ nm are rejected because these

are representative of "hot" pixels since their PSF are too narrow for a single-molecule event (the ideal, theoretical σ_x, σ_y of the PSF of a resorufin product molecule is ~126 nm)[11]. Next, candidate events with their PSF width greater than 100 nm and less than a filter threshold value (σ_{filter}, usually ~220 nm, see Supplementary Figure 5 d and e) are selected as single-molecule events. For those candidate events with their PSF greater than σ_{filter} (e.g., Supplementary Figure 5 f and g where a significant population of the candidate events show broad σ_x and σ_y), if their PSF intensity is greater than the PSF intensity of a single-molecule event (see Supplementary Figure 5h), we choose them as multiple-molecule events with the number of molecules determined by the total PSF intensity divided by the PSF intensity of a single-molecule event; otherwise they are rejected as a molecule that diffused significantly on the catalyst surface (about 4% of the observed events). The calculated specific reaction rate includes single-molecule and multiple-molecule events. Additionally, if two molecules are detected in two consecutive frames and the distance between their centroid locations in these two frames is less than 100 nm (about $2\times\sqrt{Err_x^2+Err_y^2}$, see Supplementary Figure 5 i and j), these two molecules are only counted once and the centroid position of the first of the two frames is recorded, in order to avoid the overestimation of catalytic activity due to multi-frame events (about 1% of the observed events) (i.e., product molecules adsorbed on catalysts for a time longer than a single frame acquisition time).

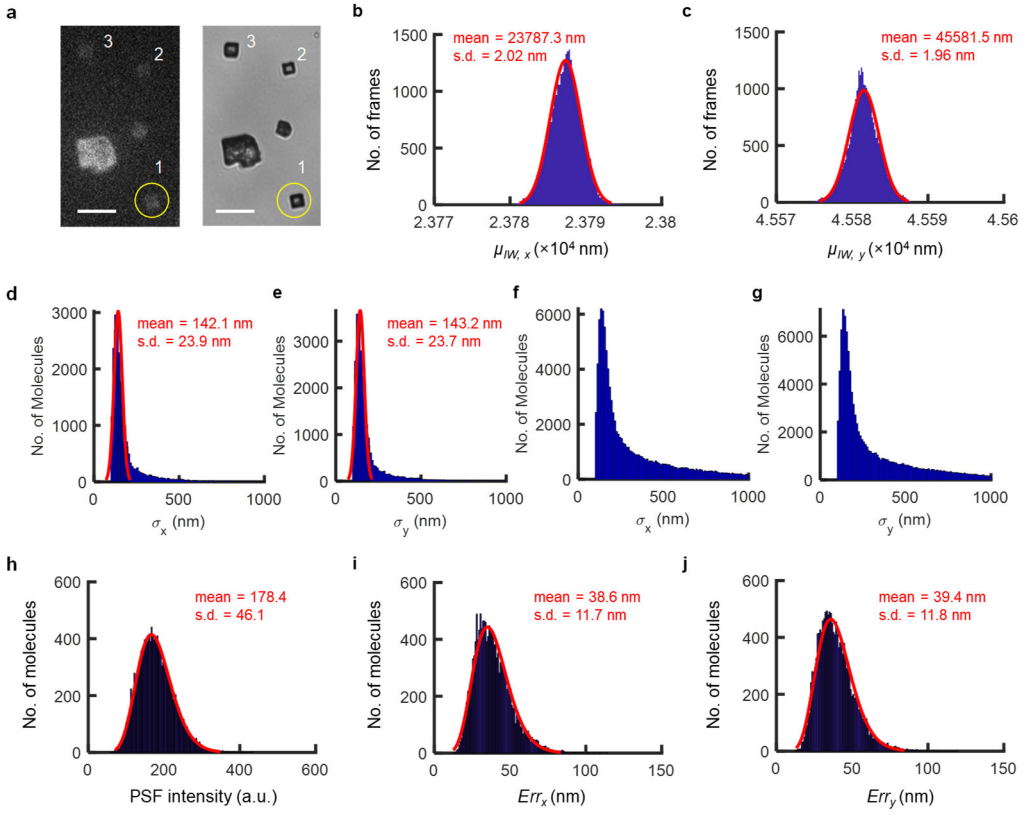

Supplementary Figure 5. Data analysis procedure for quantitative single-molecule localization and counting. **a**, Fluorescence image (left) with its corresponding optical transmission image (right), showing the intrinsic photoluminescence of $BiVO_4$ crystals (left). The object highlighted by the yellow circle is the $BiVO_4$ crystal shown in main text Fig. 2. Scale bar: 10 μm. **b-c**, Distributions of the drift-corrected $\mu_{IW,x}$ (**b**) and $\mu_{IW,y}$ (**c**) for particle 1 in **a**. Red line: fit with a Gaussian distribution. **d-e**, Distributions of σ_x (**d**) and σ_y (**e**) for particle 1 in **a** with 50 nM AR in the presence of 250 μM HQ, a condition when the majority of the candidate events are single-molecule events. Red line: fit with a Gaussian distribution for data between 100 and 200 nm. σ_{filter} is defined as the smaller value of the mean of σ_x and σ_y data between 100 and 200 nm plus three standard deviations of this Gaussian fit. **f-g**, Distributions of σ_x (**f**) and σ_y (**g**) for particle 1 in **a** with 50 nM AR in the absence of HQ, showing an example whereby a significant

population of the candidate events are multiple-molecule events, reflected by the many larger values of σ_x and σ_y (i.e., broadening of PSF). **h**, Distribution of the PSF intensity of single-molecule events for particle 1 in **a** in the absence of HQ. Red line: fit with a Gamma distribution. **i-j**, Distributions of Err_x (**i**) and Err_y (**j**) of single-molecule events for particle 1 in **a** in the absence of HQ. Red line: fit with a Gamma distribution.

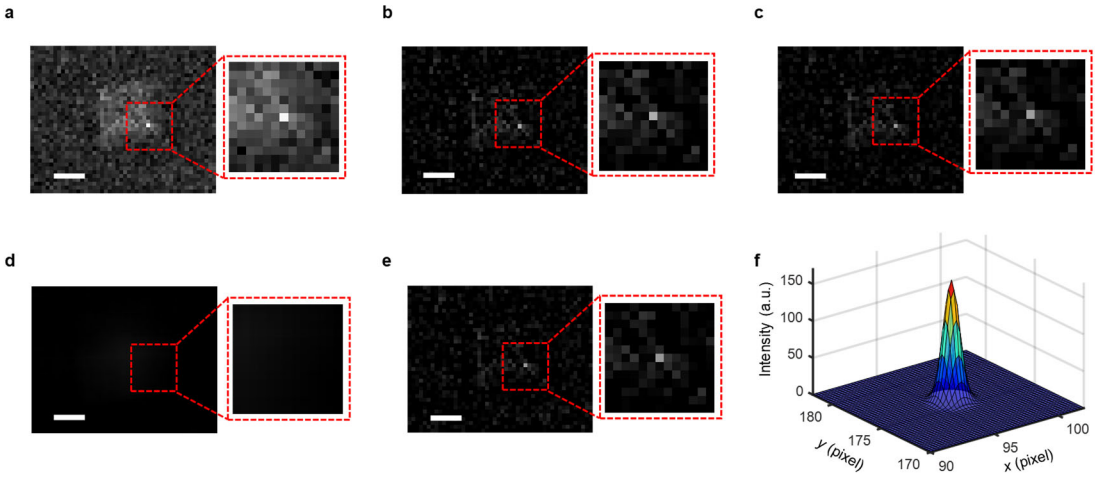

Supplementary Figure 6. Representative image processing procedure for spot localization of individual fluorescent product molecules. **a**, Original fluorescence image. **b**, $BiVO_4$ photoluminescence-subtracted image of **a**. **c**, Low-pass Gaussian-smoothed image of **b**. **d**, Spatially non-uniform background image estimated from **c** using boxcar kernel. **e**, Final image for single-molecule localization produced by subtracting **d** from **c**. **f**, two-dimensional Gaussian PSF fitting of a selected 13×13 pixel^2 area in **e** (i.e., the red square) for localization of each fluorescent product molecule. All scale bars: 2 μm.

1.4.2. *Overlay of SEM structural contour onto optical microscopy (OM) transmission image (and the super-resolution catalysis image), with ~7 nm overlay error*

Our COMPEITS imaging experiments were performed in regions with easily identifiable objects in both SEM and OM images, which enabled a straightforward correlation between the OM and SEM images (see Supplementary Figure 7 a(I) and b(I)). For a $BiVO_4$ crystal with a well-defined tetragonal bifrustum morphology, we can clearly see its rectangular structural contour in both the SEM and OM images, and can easily establish the correspondence between the vertices of the SEM rectangular structural contour and the vertices of the OM rectangular structural contour. Briefly, we determine the center position and orientation of each individual $BiVO_4$ crystal from OM and SEM images by fitting its structure contour with a rectangle, and then perform the overlaying procedure based on the OM- and SEM-determined center positions and orientations. The overlay procedure for each individual $BiVO_4$ crystal is based upon establishing a transformation relation from the OM image to the SEM image. Such transformation involves both translational and rotational moves. Therefore, the overall overlay error is associated with the translational error and the rotational error. The detailed overlay procedure is described in the following.

For the SEM image processing, we first obtain a high-resolution SEM image of the target BiVO4 crystal (Supplementary Figure 7a(II), pixel size = 7.3 nm), which then undergoes a MATLAB built-in edge detection algorithm with the Canny method to identify the outer and inner rectangular structural contours that corresponds to the outside peripheries of the {110} and {010} facets, respectively. The outer rectangular contour is continuous, and can be filled to create a binary mask, which is then fitted with a rectangle using the least squares regression method (Supplementary Figure 7a(III)). The inner rectangular contour is directly fitted with a rectangle using the least squares regression method (Supplementary Figure 7a(IV)). The parameters L and S are calculated as the square root of the area of outer and inner fitted

rectangle, respectively. The shape parameter ξ is defined as $\xi = S / L$. Supplementary Figure 7a(V) overlays the fitted outer and inner rectangles with the original high-resolution SEM image.

For the OM image processing, the OM transmission image is first expanded by four times through bicubic interpolation (Supplementary Figure 7b(II)), and then undergoes a MATLAB built-in edge detection algorithm with the Canny method to identify the rectangular structural contour. This continuous structural contour is then filled to generate a binary mask, which is subsequently fitted with a rectangle using the least squares regression method (Supplementary Figure 7b(III)). Supplementary Figure 6b(IV) overlays the fitted outer rectangle with the expanded OM transmission image. Note that the OM transmission image is diffraction-limited in resolution, and thus we do not use its fitted rectangle to report the size of the crystal, which is better determined from the SEM image. Nevertheless, the center position and the orientation of the crystal in the OM image can be accurately determined by this fitted rectangle. By overlaying the SEM- and OM-determined center positions and aligning the SEM- and OM-determined orientations, we can map the SEM structural contour onto the OM transmission image, as well as on the super-resolution catalysis image of fluorescent reaction products, which share the exact same coordinate system with the OM transmission image. Therefore, we can determine the position of each product molecule on each crystal relative to the crystal's identified different types of facets and edge-like regions (see main text Figs. 2, f and g).

From here on, we describe the detailed procedure of evaluating the overlay error. As discussed earlier, the overlay involves both translation and rotation, which are based upon the center positions and orientations of the fitted rectangles, respectively. Since the center position and orientation of a rectangle is determined by the positions of the four vertices, the overlay error is governed by the uncertainty in the vertex position. In other words, the translational error and rotational error originate from the errors in the determined vertex positions of the fitted rectangles in the SEM and OM images. Additionally, note that the center position and orientation of the crystal in the SEM image are determined by the outer, instead of the inner, rectangular structural contour, because the outer contour directly corresponds to the structural contour identified in the OM image. Specifically, the center position of the rectangle PQRS shown in Supplementary Figure 7a(V) should be overlaid with the center position of the rectangle P'Q'R'S' shown in Supplementary Figure 7b(IV), and the orientations of these two rectangles should be aligned. Supplementary Figure 7c illustrates schematically the overlay routine, the error of which can be calculated by the following steps.

Step 1. Estimation of the vertex position error

First we quantify the error in the x and y position for the eight vertices of the two rectangles (Δx_P, Δx_Q, Δx_R, Δx_S, Δy_P, Δy_Q, Δy_R, Δy_S for the SEM image; $\Delta x_{P'}$, $\Delta x_{Q'}$, $\Delta x_{R'}$, $\Delta x_{S'}$, $\Delta y_{P'}$, $\Delta y_{Q'}$, $\Delta y_{R'}$, $\Delta y_{S'}$ for the OM image) by calculating the averaged range of x and y when the fitting quality decreases by 50% (i.e., the norm of the residual increases by 50% relative to the original minimum value from the least squares regression). The calculated error of each vertex position in the SEM and OM images is listed in Supplementary Table 1.

Step 2. Estimation of the translational error

Next we estimate the translational error (Δr). The center position of the crystal in the SEM image (x_{center}^{SEM}, y_{center}^{SEM}) is determined by:

$$x_{center}^{SEM} = \frac{x_P + x_Q + x_R + x_S}{4} \qquad \text{Eq. S9}$$

$$y_{center}^{SEM} = \frac{y_P + y_Q + y_R + y_S}{4} \qquad \text{Eq. S10}$$

Similarly, the center position of the crystal in the OM image (x_{center}^{OM}, y_{center}^{OM}) is determined by:

$$x_{center}^{OM} = \frac{x_{P'} + x_{Q'} + x_{R'} + x_{S'}}{4} \quad \text{Eq. S11}$$

$$y_{center}^{OM} = \frac{y_{P'} + y_{Q'} + y_{R'} + y_{S'}}{4} \quad \text{Eq. S12}$$

Therefore, the errors in the center positions in the SEM image (Δx_{center}^{SEM}, Δy_{center}^{SEM}) and OM image (Δx_{center}^{OM}, Δy_{center}^{OM}) can be calculated as:

$$\Delta x_{center}^{SEM} = \sqrt{\frac{(\Delta x_P)^2 + (\Delta x_Q)^2 + (\Delta x_R)^2 + (\Delta x_S)^2}{4^2}} \quad \text{Eq. S13}$$

$$\Delta y_{center}^{SEM} = \sqrt{\frac{(\Delta y_P)^2 + (\Delta y_Q)^2 + (\Delta y_R)^2 + (\Delta y_S)^2}{4^2}} \quad \text{Eq. S14}$$

$$\Delta x_{center}^{OM} = \sqrt{\frac{(\Delta x_{P'})^2 + (\Delta x_{Q'})^2 + (\Delta x_{R'})^2 + (\Delta x_{S'})^2}{4^2}} \quad \text{Eq. S15}$$

$$\Delta y_{center}^{OM} = \sqrt{\frac{(\Delta y_{P'})^2 + (\Delta y_{Q'})^2 + (\Delta y_{R'})^2 + (\Delta y_{S'})^2}{4^2}} \quad \text{Eq. S16}$$

Since the translational distance *r* is the distance between the two center points (i.e., $r_x = x_{center}^{SEM} - x_{center}^{OM}$ and $r_y = y_{center}^{SEM} - y_{center}^{OM}$), the errors in r_x and r_y (Δr_x, Δr_y) are determined by:

$$\Delta r_x = \sqrt{(\Delta x_{center}^{SEM})^2 + (\Delta x_{center}^{OM})^2} \quad \text{Eq. S17}$$

$$\Delta r_y = \sqrt{(\Delta y_{center}^{SEM})^2 + (\Delta y_{center}^{OM})^2} \quad \text{Eq. S18}$$

And lastly, the total error in *r* is estimated by

$$\Delta r = \sqrt{(\Delta r_x)^2 + (\Delta r_y)^2} \quad \text{Eq. S19}$$

The calculated errors at each step for evaluating the uncertainty in the translational move are summarized in Supplementary Table 1.

Step 3. Estimation of the rotational error

Here we estimate the rotational error. The orientation of the crystal in the SEM and OM images can be determined by any combination of two different vertices of the fitted rectangle. The rotational angel determined by any combination ($\alpha = \theta - \theta'$, also see Supplementary Figure 7c) is equivalent. However, since the position error for each vertex is different, the error in the rotation angel ($\Delta\alpha$) is dependent on the specific pair of vertices employed. There are six different combinations, and the rotational error is the value averaged over these combinations.

For each combination of vertices (using P, S in the SEM image versus P', S' in the OM image as an example), the rotational error can be estimated as the following.

Since the orientation in the SEM image (θ) is determined by

$$\tan\theta = \frac{y_S - y_P}{x_S - x_P} \qquad \text{Eq. S20}$$

The error in $\tan\theta$ is calculated as

$$\Delta(\tan\theta) = \left|\tan\theta\right| \sqrt{\left(\frac{\left(\Delta\left(y_S - y_P\right)\right)^2}{\left(y_S - y_P\right)^2}\right) + \left(\frac{\left(\Delta\left(x_S - x_P\right)\right)^2}{\left(x_S - x_P\right)^2}\right)} \qquad \text{Eq. S21}$$

where

$$\Delta\left(y_S - y_P\right) = \sqrt{\left(\Delta y_S\right)^2 + \left(\Delta y_P\right)^2} \qquad \text{Eq. S22}$$

$$\Delta\left(x_S - x_P\right) = \sqrt{\left(\Delta x_S\right)^2 + \left(\Delta x_P\right)^2} \qquad \text{Eq. S23}$$

Note that the partial derivative of an inverse tangent function, $f(\chi) = \tan^{-1}(\chi)$, is $\frac{df}{d\chi} = \frac{1}{1+\chi^2}$.

Therefore, the error in θ (i.e., $\Delta\theta$) is calculated as

$$\Delta\theta = \frac{\Delta(\tan\theta)}{1+(\tan\theta)^2} \qquad \text{Eq. S24}$$

In a similar way, the error in the orientation of the crystal in the OM image ($\Delta\theta'$) can be determined. Since the rotation angle is determined by $\alpha = \theta - \theta'$, the total rotational error ($\Delta\alpha$) is calculated as:

$$\Delta\alpha = \sqrt{\left(\left\langle\Delta\theta\right\rangle\right)^2 + \left(\left\langle\Delta\theta'\right\rangle\right)^2} \qquad \text{Eq. S25}$$

where $\left\langle\Delta\theta\right\rangle$ and $\left\langle\Delta\theta'\right\rangle$ are the averaged values from all the six different combinations of vertices.

The calculated errors for each combination of vertices for evaluating the uncertainty in the rotational move are summarized in Supplementary Table 1.

Step 4. Estimation of the overall overlay error

Therefore, the overall overlay error (ΔD) that consider both translational and rotational errors is determined by

$$\Delta D = \sqrt{(\Delta r)^2 + (d\Delta\alpha)^2} \qquad \text{Eq. S26}$$

where d is the maximum distance for the rotation, which is the distance between the center and the vertex of the fitted rectangle in the SEM image (see Supplementary Figure 7c).

Pooling results from the 42 particles measured in this study, the distributions of the translational error (i.e., Δr), the rotational error (i.e., $\Delta\alpha$), and the overlay error (i.e., ΔD) are shown in Supplementary Figure 8, a – c, respectively. Therefore, as shown in Supplementary Figure 8c, ***the overall overlay error is estimated to be 6.85 nm, i.e., ~7 nm, which is negligible compared to the spatial resolution of our catalysis imaging experiments (~40 nm, see Supplementary Figure 5, i and j)***.

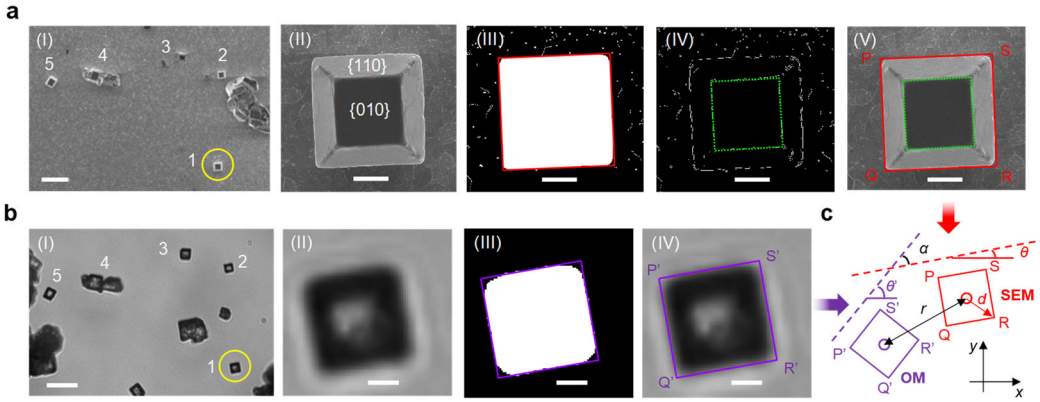

Supplementary Figure 7. Procedure of overlaying the SEM-determined crystal structural contour onto the OM transmission image. a, Determination of the center position and orientation of a single $BiVO_4$ crystal from its SEM image. (aI) Low-magnification SEM image with five identifiable objects (labelled as 1, 2, 3, 4, and 5). The object highlighted by the yellow circle is the target $BiVO_4$ crystal, which is shown in main text Fig. 2. Scale bar: 10 μm. (aII) High-resolution SEM image of the target crystal with the {010) and {110) facets labelled. Scale bar: 1 μm. (aIII) Binary image of (aII) after edge detection and filling of the connected regions, showing the filled area that corresponds to the outside periphery of the {110) facet, together with the fitted rectangle (red line). Scale bar: 1 μm. (aIV) Binary image after edge detection showing the inner structure contour that corresponds to the periphery of the {010) facet, together with the fitted rectangle (green dash line). Scale bar: 1 μm. (aV) Overlay of (aII) with the fitted outer and inner rectangles. Scale bar: 1 μm. **b**, Determination of the center position and orientation of a single $BiVO_4$ crystal from its OM transmission image. (bI) OM transmission image of the same region as panel aI with five identifiable objects (labelled as 1, 2, 3, 4, and 5). The object highlighted by the yellow circle is the target $BiVO_4$ crystal. Scale bar: 10 μm. (bII) Transmission image of the target crystal expanded 4 times in each dimension. Scale bar: 1 μm. (bIII) Binary image of bII after edge detection and filling of the connected regions, showing the filled area that corresponds to the outside periphery of the {110) facet, together with the fitted rectangle (purple line). Scale bar: 1 μm. (bIV) Overlay of bII with the fitted rectangle. Scale bar: 1 μm. **c**, Schematic illustration of the overlay procedure. The rectangles PQRS and P'Q'R'S' are drawn for the illustration purpose only, so the sizes and orientations of them do not reflect the actual values. The translational distance is indicated by r, and the rotational angle is indicated by α.

Supplementary Table 1. Summary of the calculated errors during the uncertainty propagation for the $BiVO_4$ crystal shown in Supplementary Figure 7

error of the vertex position in the SEM image (nm)[a]
$\Delta x_P = 0.076$ $\Delta x_Q = 0.079$ $\Delta x_R = 0.013$ $\Delta x_S = 0.015$
$\Delta y_P = 1.02$ $\Delta y_Q = 0.53$ $\Delta y_R = 0.52$ $\Delta y_S = 1.37$
error of the vertex position in the OM image (nm)

$\Delta x_{P'} = 4.71$ $\Delta x_{Q'} = 0.98$ $\Delta x_{R'} = 0.26$ $\Delta x_{S'} = 0.33$ $\Delta y_{P'} = 6.19$ $\Delta y_{Q'} = 0.99$ $\Delta y_{R'} = 2.34$ $\Delta y_{S'} = 9.91$	
translational error (nm)	**rotational error (°)**
$\Delta x_{center}^{SEM} = 0.027$ $\Delta y_{center}^{SEM} = 0.46$ $\Delta x_{center}^{OM} = 1.21$ $\Delta y_{center}^{OM} = 2.98$	P/Q and P'/Q': $\Delta\theta = 0.0022$ $\Delta\theta' = 0.076$ P/R and P'/R': $\Delta\theta = 0.011$ $\Delta\theta' = 0.067$ P/S and P'/S': $\Delta\theta = 0.031$ $\Delta\theta' = 0.18$ Q/R and Q'/R': $\Delta\theta = 0.013$ $\Delta\theta' = 0.039$ Q/S and Q'/S': $\Delta\theta = 0.013$ $\Delta\theta' = 0.064$ R/S and R'/S': $\Delta\theta = 0.0012$ $\Delta\theta' = 0.028$
$\Delta r_x = 1.21$ $\Delta r_y = 3.03$	
$\Delta r = 3.25$	$\Delta\alpha = 0.077$
overall overlay error (nm)	
$\Delta D = 4.42$	

[a] Note: the errors of the vertex positions in the SEM image being significantly smaller in the *x* axis than in the *y* axis is due to the orientation and the detected edge points of this particular particle.

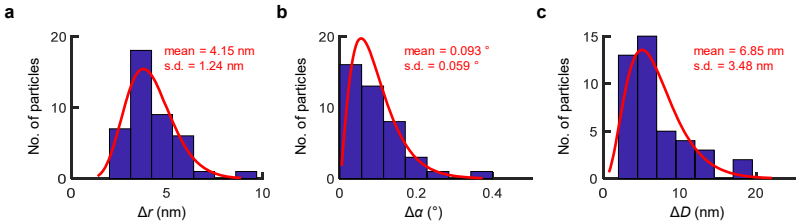

Supplementary Figure 8. Distributions of the estimated overlay errors for Δr (**a**), $\Delta\alpha$ (**b**) and ΔD (**c**) for the 42 particles measured in our study. Red line: fit with a Gamma distribution.

1.4.3. *Quantification of the specific reaction rate at single-particle and sub-particle levels*

1.4.3.1. Image segmentation and calculation of the specific reaction rate

The detailed procedure of calculating the specific reaction rate for the whole $BiVO_4$ crystal, {010} basal facet, {110} lateral facet, type I edge, and type II edge are summarized in Supplementary Table 2 and Supplementary Table 3. Briefly, for each individual $BiVO_4$ crystal, the peripheries of the outer and inner rectangles can be determined from its SEM image, and mapped onto the corresponding super-resolution catalysis image based on the methodology described in Section 1.4.2. Next, the catalysis image is dissected into several sub-particle regions. The structural contours determined from SEM images allow for calculating the actual surface areas on the 3-D crystal using the known geometry of the crystal (see Supplementary Table 3). Additionally, the effect on the reaction rate of the light intensity difference between facets that encounter the incident light in opposite ways can be corrected by numerical simulations using the semiconductor charge carrier drift-diffusion model (see Supplementary Table 3 and Section 1.4.3.2).

Supplementary Table 2. Calculation of specific reaction rate for single particles and for different sub-particle regions

	Total area of interest	Area dissection	Calculation of specific rate
Whole particle	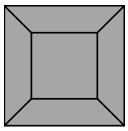	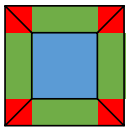	$v = \frac{N_b f_b + N_g f_g + N_r f_r}{(A_b + A_g + A_r)t}$
Basal {010} facet	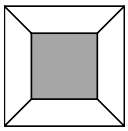	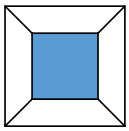	$v = \frac{N_b f_b}{A_b t}$
Lateral {110}1 facet	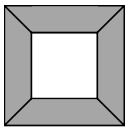	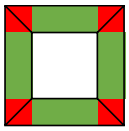	$v = \frac{N_g f_g + N_r f_r}{(A_g + A_r)t}$
Type-I edge	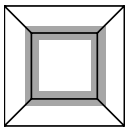	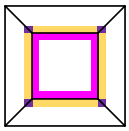	$v = \frac{N_m f_m + N_o f_o + N_p f_p}{(A_m + A_o + A_p)t}$
Type-II edge	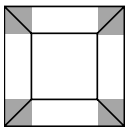	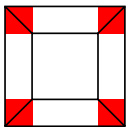	$v = \frac{N_r f_r}{A_r t}$

Notes: (1) The subscript b, g, r, o, p and m indicates the blue, green, red, orange, purple, and magenta region, respectively. (2) N is the number of observed reactions, including both the single-molecule and multiple molecule events. (3) A_i (i = b, g, r, o, p, or m) is the surface area of the indicated region for the top half of the $BiVO_4$ particle, the calculation of which are summarized in Supplementary Table 3. (4) t is the time duration of the movie (i.e., the imaging experiment). (5) f_i (i = b, g, r, o, p, or m) are correction factors, the definition and calculation of which are summarized in Supplementary Table 3. (6) The outmost periphery of the projected square also represents a type-II edge, which, by definition, is the edge between two neighboring lateral {110} facets and here between one top and one bottom lateral facet. We did not analyze this outmost periphery because the top and bottom lateral facets have different illumination conditions and type-II edge region is already represented as defined in this table.

Supplementary Table 3. Calculation of the surface area and the light attenuation correction factor for quantification of specific reaction rate

	Surface area A_i	Light attenuation correction factor f_i
Blue region	$A_b = S^2$	$f_b = 1$
Green region	$A_g = 2\sqrt{2}S(L-S)$	$f_g = \dfrac{\eta}{\eta + \int_0^{\eta} r(\lambda)\, d\lambda}$
Red region	$A_r = \sqrt{2}(L-S)^2$	$f_r = \dfrac{\frac{\eta^2}{2\sqrt{2}}}{\frac{\eta^2}{2\sqrt{2}} + \int_0^{\eta} r(\lambda)\left(\frac{\eta-\lambda}{\sqrt{2}}\right) d\lambda}$
Orange region	$A_o = 4\sqrt{2}Sw$	$f_o = \dfrac{w\sqrt{2}}{w\sqrt{2} + \int_{\eta - w\sqrt{2}}^{\eta} r(\lambda)\, d\lambda}$
Purple region	$A_p = 4\sqrt{2}w^2$	$f_p = \dfrac{\frac{w^2}{\sqrt{2}}}{\frac{w^2}{\sqrt{2}} + \int_{\eta - w\sqrt{2}}^{\eta} r(\lambda)\left(\frac{\eta-\lambda}{\sqrt{2}}\right) d\lambda}$
Magenta region	$A_m = S^2 - (S-2w)^2$	$f_m = 1$

Notes: (1) $r(\lambda)$ is a function from numeric simulations defined in 1.4.3.2. (2) η is an introduced auxiliary parameter determined by the size and shape parameters (L, ζ), and is defined as $\eta = \frac{L(1-\xi)}{\sqrt{2}}$. It is the distance between the two parallel edges of the lateral facet and is shown in Supplementary Figure 9b. (3) w is the width of the blue or orange ribbon in the definition of type-I edge (see Supplementary Table 2), and a value of 50 nm was chosen that is slightly larger than the single-molecule localization error (~40 nm, see Supplementary Figure 5, i and j) in our imaging experiments.

1.4.3.2. Calculation of light attenuation correction factor

In our imaging experiments, the incident 405-nm laser travels in a direction that is passing the $BiVO_4$ crystal first and then reaches the ITO electrode (Supplementary Figure 9a). Based on the crystal structure of monoclinic $BiVO_4$ (a = 5.1035 Å, b = 5.0898 Å, c = 11.6972 Å, α = 90°, β = 90.387°, γ = 90°)[12], the angle ϕ between the basal and lateral facets can be determined to be 45.027° (i.e., ≈ 45°) by either of the two equivalent methods discussed below.

First, the crystal vector (i.e., Miller index, hkl) in the monoclinic crystal system is converted to the crystal vector in the Cartesian space ($h'k'l'$) using the following equation:

$$\begin{bmatrix} h' \\ k' \\ l' \end{bmatrix} = \begin{bmatrix} a\sin\beta & b\sin\alpha\cos\delta & 0 \\ 0 & b\sin\alpha\sin\delta & 0 \\ a\cos\beta & b\cos\alpha & c \end{bmatrix} \times \begin{bmatrix} h \\ k \\ l \end{bmatrix} \quad \text{Eq. S27}$$

where δ is determined by

$$\cos\delta = \frac{\cos\gamma - \cos\alpha\cos\beta}{\sin\alpha\sin\beta} \quad \text{Eq. S28}$$

Next, the angle (ϕ) between two crystal planes 1 and 2 can be determined using their Cartesian crystal vectors ($h_1'k_1'l_1'$) and ($h_2'k_2'l_2'$) based on the following equation:

$$\cos\phi = \frac{h_1'h_2' + k_1'k_2' + l_1'l_2'}{\sqrt{\left(h_1'^2 + k_1'^2 + l_1'^2\right)\left(h_2'^2 + k_2'^2 + l_2'^2\right)}} \quad \text{Eq. S29}$$

Alternatively, the angle ϕ can also be calculated directly using the Miller indices in the monoclinic crystal system ($h_1k_1l_1$) and ($h_2k_2l_2$) based on the following equation:

$$\cos\phi = \frac{d_1d_2}{\sin^2\beta}\left[\frac{h_1h_2}{a^2} + \frac{k_1k_2\sin^2\beta}{b^2} + \frac{l_1l_2}{c^2} - \frac{\left(l_1h_2 + l_2h_1\right)\cos\beta}{ac}\right] \quad \text{Eq. S30}$$

where d is the D-spacing for each crystal plane, and is determined by

$$\frac{1}{d^2} = \frac{1}{\sin^2\beta}\left[\frac{h^2}{a^2} + \frac{k^2\sin^2\beta}{b^2} + \frac{l^2}{c^2} - \frac{2hl\cos\beta}{ac}\right] \quad \text{Eq. S31}$$

The light intensity at the top basal {010} facet and the top lateral {110} facet is equal. However, the light intensity at the bottom lateral {110} facet is different from that at the top facets due to the significant absorption of 405-nm light by the $BiVO_4$ crystal (the value of absorption coefficient is shown in Supplementary Table 4). Also, the light intensity at the bottom basal {010} facet is different from that at the top facets but it does not require correction since the bottom basal {010} facet, which is in direct contact with the ITO, is not accessible by the reaction solution (Supplementary Figure 9a), and therefore does not participate in catalyzing surface reactions (even if it does, it does not change the value of K_{HQ} extracted from our data analysis, as this correction is the same across all [HQ] concentration and does not change the [HQ] dependence of v_{AR}, from which K_{HQ} is derived).

In order to compare faithfully the reactivity between the basal and lateral facets, we need to include only the reactions that occur at the top {010} and {110} facets when calculating the specific reaction rate. In other words, the reactions occurring at the bottom {110} facet that is closer to ITO should be factored out. To do this, we quantify the ratio of the expected number of product molecules between the top and bottom {110} facets, based on the differences in the light intensity and illumination configuration between these two facets. Such differences lead to different surface hole fluxes between these two facets, which, in turn, lead to different numbers of AR oxidation reactions.

It should be noted that in this study the specific reaction rates are calculated taking into account the light attenuation correction factors in order to reflect faithfully the AR oxidation activities of the top {010} and {110} facets of a $BiVO_4$ particle illuminated with identical laser intensities. Nevertheless, such

correction does not affect the determination of K_{AR} and K_{HQ} at all since it only affects the magnitudes of the fitted titration curves (Fig. 2 h – k) but not the dependences on [AR] or [HQ], which determine the K_{AR} and K_{HQ}.

Here we define $r(\lambda)$ as the ratio of surface hole flux between the top and bottom {110} facets with the λ-coordinate defined in Supplementary Figure 9a. It is easy to understand that this ratio is dependent on λ since at different λ values, the vertical distance H for the light attenuation is different. The surface hole flux can be calculated by numeric simulation of the semiconductor charge carrier behavior [13], as detailed in the following.

The hole continuity equation is solved to obtain the free hole concentration (p) inside the $BiVO_4$ crystal as a function of the distance (z; the z-coordinate is defined in Supplementary Figure 9a) away from the semiconductor/electrolyte interface (SEI).

The governing equation for p as a function of z and time (t) is

$$\frac{\partial p}{\partial t} = -\frac{1}{q}\frac{\partial j_{\mathrm{h}}}{\partial z} + G_{\mathrm{h}}(z) - R_{\mathrm{h}}(z) \qquad \text{Eq. S32}$$

where q is the elementary charge, j_{h} is the hole current density (= hole flux × elementary charge), and $G_{\mathrm{h}}(z)$ and $R_{\mathrm{h}}(z)$ are the generation and recombination rate of holes, respectively. The hole current density j_{h} is expressed as

$$j_{\mathrm{h}} = -qD_{\mathrm{h}}\frac{\partial p}{\partial z} - q\mu_{\mathrm{h}}p\frac{\partial \phi}{\partial z} \qquad \text{Eq. S33}$$

where D_{h} and μ_{h} are the hole diffusion constant and the hole mobility, respectively. $\phi_{\mathrm{a}}(z)$ is the local electrostatic potential distribution inside the semiconductor, and is given by the analytical solution of the Poisson's equation:

$$\phi(z) = \phi_{\mathrm{b}} - \mathrm{sign}(V_{\mathrm{sc}})\frac{qN_{\mathrm{D}}}{2\varepsilon_0\varepsilon_{\mathrm{r}}}(w-z)^2, 0 < z < w \qquad \text{Eq. S34}$$

$$\phi(z) = \phi_{\mathrm{b}}, z > w \qquad \text{Eq. S35}$$

where ϕ_{b} is the local electrostatic potential in the semiconductor bulk, V_{sc} is the potential drop in the semiconductor relative to the surface, N_{D} is the donor concentration, ε_0 is the vacuum permittivity, and ε_{r} is the relative permittivity, and w is the width of the space charge region:

$$w = \sqrt{\frac{2\varepsilon_0\varepsilon_{\mathrm{r}}}{qN_{\mathrm{D}}}V_{\mathrm{sc}}} \qquad \text{Eq. S36}$$

The hole generation term $G_{\mathrm{h}}(z)$ is given by the Lambert-Beer law. For the top {110} facet,

$$G_{\mathrm{h}}(z) = \alpha P e^{-\alpha z} \qquad \text{Eq. S37}$$

and for the bottom {110} facet,

$$G_{\mathrm{h}}(z) = \alpha P e^{-\alpha(H-z)} \qquad \text{Eq. S38}$$

where α is the absorption coefficient, and P is the photon flux calculated from the incident light power density (120 W/cm^2), H is the vertical distance between the top and bottom {110) facets that depends on λ (see Supplementary Figure 9a). Note that for both cases $z = 0$ corresponds to the SEI, and $z > 0$ indicates the semiconductor bulk. The recombination term $R_{\mathrm{h}}(z)$ is calculated as the following by assuming direct band-to-band nonlinear recombination:

$$R_{\mathrm{h}}(z) = \frac{1}{N_{\mathrm{D}}\tau_{\mathrm{h}}}\left(n_{\mathrm{dark}}\, p - n_i^{\,2}\right) \qquad \text{Eq. S39}$$

where τ_{h} is the hole lifetime, and n_{dark} is the concentration of free electrons in the dark, and can be calculated as

$$n_{\mathrm{dark}}(z) = n_{0\mathrm{i}} \exp\left[\frac{\phi(z) - \phi_{\mathrm{b}}}{V_{\mathrm{th}}}\right] \qquad \text{Eq. S40}$$

where $n_{0\mathrm{i}}$ is the equilibrium concentration of electrons in the isolated semiconductor, and V_{th} is the thermal voltage. The hole flux at the SEI is described by a first-order approximation[13,14]:

$$F_{\mathrm{h,SEI}} = k_{\mathrm{trh}}\left(p(z=0) - p_{\mathrm{dark}}(z=0)\right) \qquad \text{Eq. S41}$$

where k_{trh} is the hole transfer rate constant, and p_{dark} is the concentration of free electrons in the dark, and can be calculated as

$$p_{\mathrm{dark}}(z) = p_{0\mathrm{i}} \exp\left[\frac{-\phi(z) + \phi_{\mathrm{b}}}{V_{\mathrm{th}}}\right] \qquad \text{Eq. S42}$$

Hence, the $r(\lambda)$ function used in Supplementary Table 3 can be calculated as

$$r(\lambda) = \frac{F_{\mathrm{h,SEI}}^{\mathrm{bottom}\{110\}}}{F_{\mathrm{h,SEI}}^{\mathrm{top}\{110\}}} \qquad \text{Eq. S43}$$

where $F_{\mathrm{h,SEI}}^{\mathrm{top}\{110\}}$ and $F_{\mathrm{h,SEI}}^{\mathrm{bottom}\{110\}}$ are the SET hole flux for the top and bottom {110} facets, respectively, at a given λ value. Note that while the value of k_{trh} is unknown, it cancels out when calculating the $r(\lambda)$ function. Supplementary Figure 9b illustrates the aerial view (see Supplementary Figure 9a, bird's-eye angle) of a top {110} facet, showing the important geometric relations and the λ-coordinate. The values of material parameters of $BiVO_4$ used in the calculation are summarized in Supplementary Table 4.

Representative hole concentration profiles as functions of z and t by solving the hole continuity equation (Eq. S32) for a selected spot (S1) at the top {110} facet and the corresponding spot (S2) at the bottom {110} facet are shown in Supplementary Figure 9 d and e, respectively. The distance of the light attenuation pathway (i.e., the vertical distance between S1 and S2) is 676 nm, corresponding to half of the height of the $BiVO_4$ crystal shown in main text Fig. 2. It can be seen from Supplementary Figure 9 d and e that for both cases, as expected, the photoexcited hole concentration is significantly higher at the SEI (i.e., $z = 0$ nm) and reaches the steady state within about 0.1 μs. When calculating the $r(\lambda)$ function, a sufficiently long time (1 s) is chosen to represent the steady state behavior, under which our experiments were carried out. By comparing Supplementary Figure 9d with Supplementary Figure 9e, it is clear that the surface hole concentration is significantly lower at the bottom {110}facet than at the top {110} facet. Supplementary Figure 9f shows the calculated $r(\lambda)$ function with the λ value range for the $BiVO_4$ crystal shown in main text Fig. 2 (0 – 955 nm).

The light attenuation correction factor (i.e., f_i) can be derived from the $r(\lambda)$ function based on the geometry of the $BiVO_4$ crystals (see Supplementary Figure 9 a – c). Recall that $r(\lambda)$ is the ratio of surface hole flux between the bottom and top {110} facets. At different λ values, the $r(\lambda)$ value is different because of the difference in the distance of the light attenuation pathway. In order to calculate the f_i factor for each of these regions specified in Supplementary Table 3, we need to first obtain the averaged r value for each region (r_{avg}) based on its geometry, and then f can be readily calculated as $f_i = 1/(1+ r_{avg})$. The integration ranges for the green, red, yellow, and purple regions in the λ-coordinate are illustrated in Supplementary Figure 9c.

The averaged r value for the green region ($r_{avg,\,g}$) is given by

$$r_{\text{avg, g}} = \frac{\int_0^{\eta} r(\lambda) \times S \times d\lambda}{S \times \eta} = \frac{\int_0^{\eta} r(\lambda)\, d\lambda}{\eta} \qquad \text{Eq. S44}$$

Therefore, it readily follows that:

$$f_{\text{g}} = \frac{1}{1 + r_{\text{avg, g}}} = \frac{\eta}{\eta + \int_0^{\eta} r(\lambda)\, d\lambda} \qquad \text{Eq. S45}$$

The averaged r value for the red region ($r_{avg,\,r}$) is given by

$$r_{\text{avg, r}} = \frac{\int_0^{\eta} r(\lambda) \times \frac{(\eta - \lambda)}{\sqrt{2}} \times d\lambda}{\frac{1}{2} \times \frac{\eta}{\sqrt{2}} \times \eta} = \frac{\int_0^{\eta} r(\lambda) \left(\frac{\eta - \lambda}{\sqrt{2}} \right) d\lambda}{\frac{\eta^2}{2\sqrt{2}}} \qquad \text{Eq. S46}$$

Therefore, it follows that:

$$f_r = \frac{1}{1 + r_{\text{avg, r}}} = \frac{\frac{\eta^2}{2\sqrt{2}}}{\frac{\eta^2}{2\sqrt{2}} + \int_0^{\eta} r(\lambda) \left(\frac{\eta - \lambda}{\sqrt{2}} \right) d\lambda} \qquad \text{Eq. S47}$$

The calculation for the yellow region is similar to that for the green region, except that the integration range is from $\eta-\sqrt{2}w$ to η instead of from 0 to η. Thus, the averaged *r* value for the yellow region ($r_{\text{avg, y}}$) is given by

$$r_{\text{avg, y}} == \frac{\int_{\eta-\sqrt{2}w}^{\eta} r(\lambda)\times S\times d\lambda}{\sqrt{2}w\times S} = \frac{\int_{\eta-\sqrt{2}w}^{\eta} r(\lambda)\,d\lambda}{\sqrt{2}w} \qquad \text{Eq. S48}$$

Therefore, it follows that:

$$f_y = \frac{1}{1+r_{\text{avg, y}}} = \frac{\sqrt{2}w}{\sqrt{2}w+\int_{\eta-\sqrt{2}w}^{\eta} r(\lambda)\,d\lambda} \qquad \text{Eq. S49}$$

Similarly, the calculation for the purple region resembles that for the green region, except that the integration range is from $\eta-\sqrt{2}w$ to η instead of from 0 to η. Thus the averaged *r* value for the purple region ($r_{\text{avg, p}}$) is given by

$$r_{\text{avg, p}} = \frac{\int_{\eta-\sqrt{2}w}^{\eta} r(\lambda)\times\left(\frac{\eta-\lambda}{\sqrt{2}}\right)\times d\lambda}{\frac{1}{2}\times\sqrt{2}w\times w} = \frac{\int_{\eta-\sqrt{2}w}^{\eta} r(\lambda)\left(\frac{\eta-\lambda}{\sqrt{2}}\right)d\lambda}{\frac{w^2}{\sqrt{2}}} \qquad \text{Eq. S50}$$

Therefore, it follows that:

$$f_p = \frac{1}{1+r_{\text{avg, p}}} = \frac{\frac{w^2}{\sqrt{2}}}{\frac{w^2}{\sqrt{2}}+\int_{\eta-\sqrt{2}w}^{\eta} r(\lambda)\left(\frac{\eta-\lambda}{\sqrt{2}}\right)d\lambda} \qquad \text{Eq. S51}$$

For the blue and magenta regions where the light attenuation correction is not needed, the f_i factor is 1.

Supplementary Table 4. Values of material parameters of $BiVO_4$ used in the calculations

Material parameter	Value
donor concentration	1×10^{18} cm^{-3} [15]
electron affinity	4.75 eV [16]
relative permittivity	68 [15]
flat band potential	0.1 V versus RHE[15]
density of states of conduction band	2.3×10^{19} cm^{-3} [15]
bandgap energy	2.4 eV [17]
hole lifetime	40 ns [18]
hole diffusion length	70 nm [18]
absorption coefficient at 405 nm	3.7×10^{4} cm^{-1} [15]

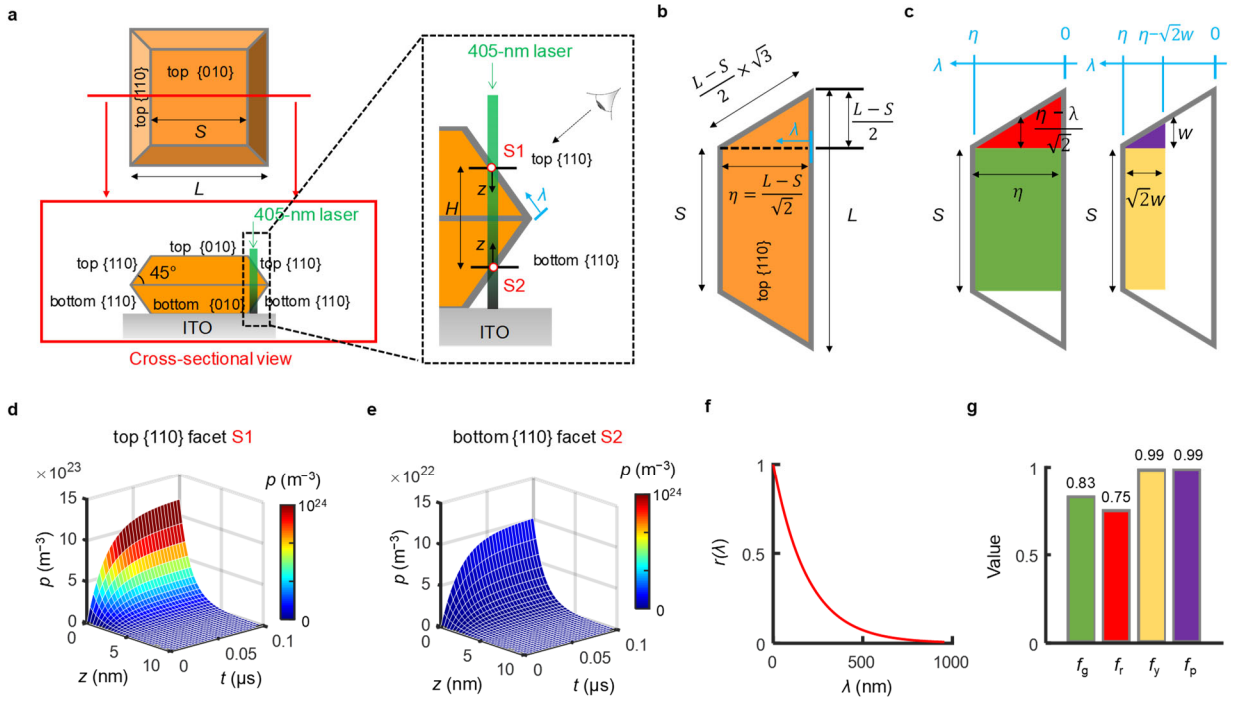

Supplementary Figure 9. Calculation of the light attenuation correction factor. a, Schematic illustration of the illumination configuration in our COMPEITS imaging experiments, the geometry of the $BiVO_4$ particle, and the definition of the z- and λ-coordinates. **b**, The aerial view (see **a**, bird's-eye angle) of a top {110} facet, showing the important geometric relations and the λ-coordinate. **c**, Illustration of the integration ranges for the green, red, yellow, and purple regions in the λ-coordinate. **d-e**, Representative hole concentration profile as functions of t and z for a selected spot (S1) at the top {110} facet (**d**) and the corresponding spot (S2) at the bottom {110) facet (**e**); S1 and S2 marked in **a**, for which $z = 0$ nm. The vertical distance (H) between S1 and S2 is 676 nm, which is half of the height of the $BiVO_4$ particle shown in main text Fig. 2. **f**, Calculated $r(\lambda)$ function with the λ value range of the $BiVO_4$ particle shown in main text Fig. 2 (0 – 955 nm; i.e., $\eta = 955$ nm). **g**, Calculated light attenuation correction factors for the green, red, yellow, and purple regions of the $BiVO_4$ particle shown in main text Fig. 2.

1.4.3.3. Effect of refraction on the light attenuation correction is minimal

We have found that taking the refraction of light into account, the light attenuation correction factors f_g, f_r, f_o, and f_p for considering the differences between top and bottom lateral facets (for the definitions of these factors, see Supplementary Table 3 and Supplementary Figure 9) only change by ~6%, ~4%, ~0.1%, and ~0.1%, respectively, as discussed later (Supplementary Figure 10). These differences are much smaller than the typical ~10% error in our measurement errors (see error bars in main text Figure 3 c-e for example). Therefore, we chose to omit the light refraction when calculating the light attenuation correct factors as an approximation in order to achieve a simpler, more feasible, mathematical manipulation during these calculations.

The refractive index of monoclinic $BiVO_4$ (clinobisvanite) is 2.45.[19] Water has a refractive index of 1.33. When the 405-nm light goes from material 1 (i.e., water, $n_1 = 1.33$) to material 2 ($BiVO_4$, $n_2 = 2.45$), the incidence angle (θ_1) and the transmission angle (θ_2) has the following relation (see Supplementary Figure 10a):

$$n_1 \sin\theta_1 = n_2 \sin\theta_2 \qquad \text{Eq. S52}$$

Since the incidence angle (θ_1) is 45° on the lateral facets, the transmission angle (θ_2) can be calculated to be 22.6°.

Each spot at the bottom-facing lateral {110} facet (e.g., the red circle shown in Supplementary Figure 10a) would have a light attenuation pathway length of H without considering light refraction (see the green solid line shown in Supplementary Figure 10a), and would have a light attenuation pathway length of H' when considering light refraction (see the green dash line shown in Supplementary Figure 10a). The relation between H and H' at any position (λ) on the lateral facet can be obtained using the Law of Sines for any triangle (see the zoomed-in triangle shown in the dash line box in Supplementary Figure 10a):

$$\frac{H(\lambda)}{\sin(90° + \theta_2)} = \frac{H'(\lambda)}{\sin(45°)} \qquad \text{Eq. S53}$$

Since $H(\lambda) = \sqrt{2}\lambda$, we can readily obtain $H'(\lambda) = \sqrt{2}\lambda \times \frac{\sin(45°)}{\sin(90° + \theta_2)}$.

Now we can calculate the attenuation degree with and without considering light refraction. Let I_0 denote the original light intensity, and I and I' denote the attenuated light intensities without and with light refraction at any given location (i.e., any given λ value), respectively. Then the light attenuation degree for the two cases ($I / I_0 = \exp(-\alpha H(\lambda))$ and $I'/ I_0 = \exp(-\alpha H'(\lambda))$) can be quantitatively compared at any location on the bottom {110} facet, and is shown in Supplementary Figure 10b.

The ratio (R_{refrac}) of the total number of photons arriving at the bottom {110} facet between the two cases (i.e., considering light refraction versus not considering light refraction) can be calculated (the definition of η is shown in Supplementary Figure 8b):

$$R_{refrac} = \frac{\int_0^{\eta} \exp(-\alpha H'(\lambda))\, d\lambda}{\int_0^{\eta} \exp(-\alpha H(\lambda))\, d\lambda} = \frac{\int_0^{\eta} \exp\left(-\alpha\sqrt{2}\lambda \times \frac{\sin(45°)}{\sin(90° + \theta_2)}\right) d\lambda}{\int_0^{\eta} \exp(-\alpha\sqrt{2}\lambda)\, d\lambda} \qquad \text{Eq. S54}$$

Then, if we consider the light refraction, the light attenuation correction factor can be estimated to be $1/(1+ r_{avg}\ R_{refrac})$, recalling that r_{avg} is the calculated ratio of the total number of AR oxidation reactions between the top and bottom {110} facets without considering light refraction. So we can estimate the four light attenuation correction factors after taking light refraction into account, and we denote these as f'_g, f'_r, f'_o, f'_p)

The relative difference for the four light attenuation correction factors between the two cases (i.e., considering light refraction versus not considering light refraction) for the 42 particles studied are expressed as $f'_g/f_g, f'_r/f_r, f'_o/f_o$, and f'_p/f_p, and the results are shown in Supplementary Figure 10 c-f. It can be readily seen that if we take the refraction of light into account, the light attenuation correction factors f_g, f_r, f_o, and f_p only decrease by ~6%, ~4%, ~0.1%, and ~0.1%, respectively. It is noted that occasionally f'_o/f_o and f'_p/f_p have values that are slightly larger than 1 resulting from numeric calculation errors from small-range (~50 nm) integrations at very large λ values (> 1000 nm), where the difference between the refraction case and non-refraction is small (see Supplementary Figure 10b).

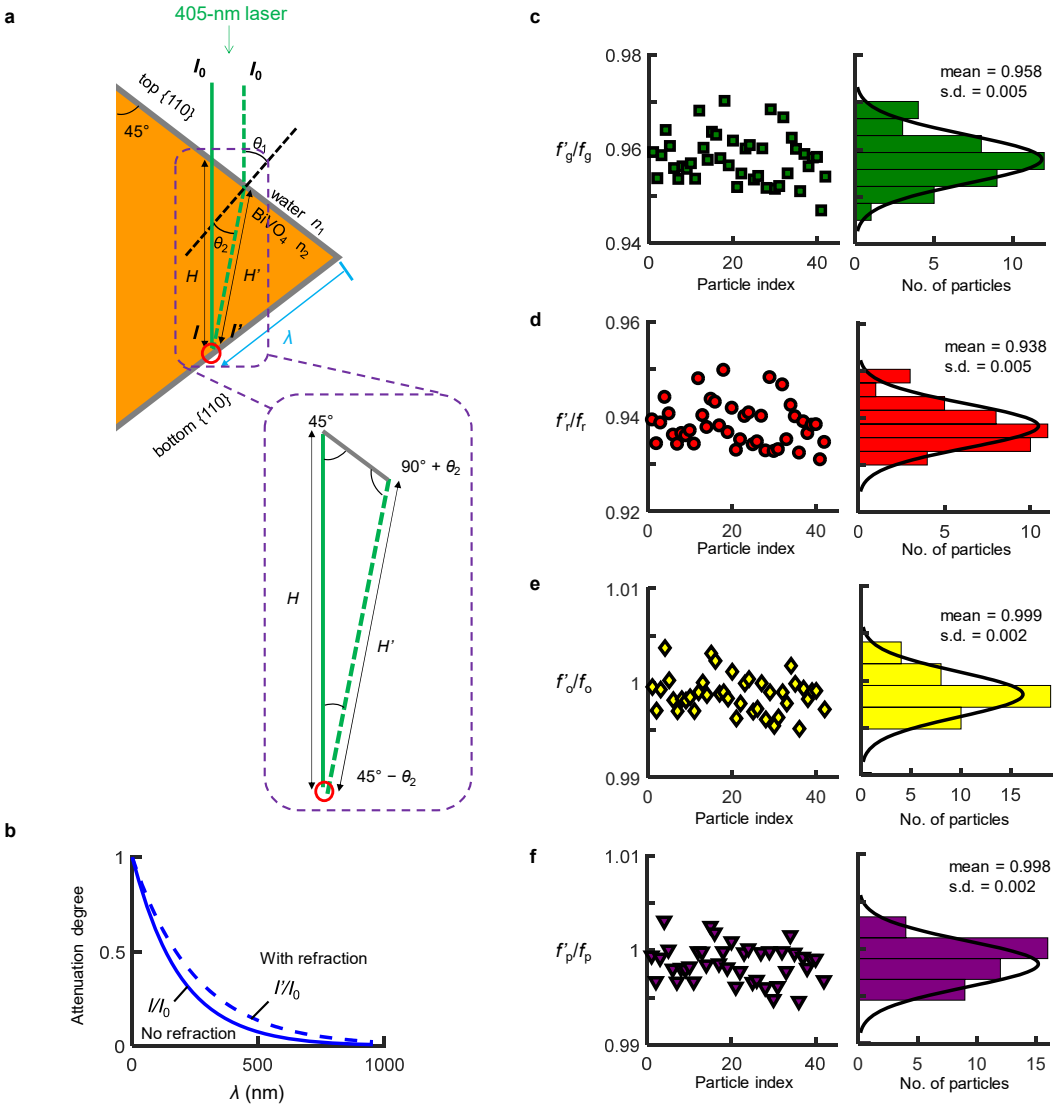

Supplementary Figure 10. Effect of light refraction on the calculation of the light attenuation correction factor for lateral facets. a, Schematic illustration of the light pathways with and without considering the refraction of light at the water/$BiVO_4$

interface. **b**, The attenuation degree (I/I_0 or I'/I_0) as a function of λ. **c** - **f**, The relative difference for the four light attenuation correction factors between the with-refraction and no-refraction cases (f'_g/f_g (**c**), f'_r/f_r (**d**), f'_o/f_o (**e**), and f'_p/f_p (**f**)) for all the 42 particles studied.

2. Additional data and discussions

2.1. Generality/applicability of COMPEITS, and significance of molecular adsorption

Generality/applicability. In principle, COMPEITS may be used to spatially map a *nonfluorescent* system that suppress, enhance the intensity of, and/or alter the emission wavelength of an auxiliary fluorescent system. Therefore, in addition to the surface reaction example investigated in this study, COMPEITS may be applicable to a wide array of nonfluorescent systems with judiciously chosen auxiliary fluorescent report processes. The target nonfluorescent process of COMPEITS could be competitions or inhibitions of surface- or enzyme-catalyzed reactions, or any processes or entities that could induce changes in fluorescence signals (e.g., intensity, wavelength, or blinking timescale), such as fluorescence quenchers and redox mediators[20-23]. The auxiliary systems could be fluorogenic reactions catalyzed by particles or enzymes, blinking molecules/particles, or any fluorescent processes that could be imaged via super-resolution microscopy. COMPEITS is certainly *not* limitless, however. It still requires an auxiliary fluorescent process as a reporter. For the HQ oxidation reaction we studied here, we could quantify its adsorption equilibrium constant, i.e., a thermodynamic property for the surface chemisorption reaction, at nanometer spatial resolution, but we cannot determine the reaction rate of the subsequent catalytic conversion of HQ to quinone.

COMPEITS would work as long as the adsorption affinities of both pro-fluorescent and nonfluorescent reactants can be accurately determined by titration (i.e.,$1/K_{AR}$ and $1/K_{HQ}$ are in experimentally titratable concentration regimes; note these K's are in inverse concentration units). Specifically, if K_{AR} or K_{HQ} is large (e.g., with $1/K$ around sub μM), it is advantageous experimentally since titrating AR or HQ concentration to ~1 μM would be sufficient to reliably determine the values of K_{AR} or K_{HQ}. However, if K_{AR} or K_{HQ} is too large (e.g., $1/K$ ~ pM to sub-nM), the adsorption of AR or HQ becomes too strong, and as a result, K_{AR} or K_{HQ} will be challenging to quantify as concentrations in the pM to sub-nM range are unreliable to maintain in solution. On the other hand, if K_{AR} or K_{HQ} is too small (e.g., 1/K ~ mM to M), a very high AR or HQ concentration would be needed to obtain a well-shaped titration curve, and the fluorescence background, if the molecule involved (i.e., AR or HQ) has any fluorescence *at all*, could become too high to achieve single-molecule detection. For molecules that have absolutely no fluorescence such as water and ethanol, there is no upper limit for their concentration ranges for titrations.

The COMPEITS strategy only requires that the pro-fluorescent substrate and non-fluorescent substrate compete for surface sites, so that the adsorption of one substrate precludes or interferes with the adsorption of the other substrate at the same surface site, which could be a single surface atom, a cluster of surface atoms, or a small surface patch, depending on the physical size of the competing substrate molecules. At the small size limit (e.g., monoatomic and diatomic molecules), this competition would require that the two substrate molecules want to adsorb onto almost the same surface atom, but for larger molecules, as long as their surface adsorption sites are close enough to cause steric interference/exclusion, competition will arise. Therefore, the physical sizes of molecules should play a role in the requirement of the type of surface adsorption sites in order for the competition to occur.

Our COMPEITS measurements characterize the thermodynamic adsorption properties of the nonfluorescent reactant HQ, and do not directly provide dynamic information about the surface migration of this molecule (since we do not directly image it). If the adsorbed nonfluorescent molecule migrates on the catalyst surface, the K_{HQ} determined would then be the *effective* adsorption equilibrium constant of the

nonfluorescent molecule at the surface site where the pro-fluorescent molecule reacts and its fluorescence is recorded. COMPEITS cannot provide information on the kinetic migration process (i.e., a time-dependent migration trajectory) of the nonfluorescent molecule. However, if the surface adsorption property evolves over time (e.g., through surface reconstruction) and if the timescale of this temporal evolution is much longer than the time needed to form a COMPEITS image, we can then extract how K_{HQ} changes over time by performing titrations in a time-segmented manner.

Significance of studying molecular adsorption by COMPEITS. It is worth noting that molecular adsorption on solid surfaces is a fundamental phenomenon that has broad implications in various fields of inquiry and plays a critical role in many chemical, physical and biological processes. Therefore, spatiotemporally-resolved quantitative information of molecular adsorption, readily obtainable via COMPEITS, would potentially offer valuable insights into a deeper understanding of these processes.

In the case of photocatalytic degradation of organics for water decontamination, the majority of aqueous contaminants are pollutants with low solubilities in water (e.g., polycyclic aromatic hydrocarbons, pesticides, pharmaceuticals and endocrine disrupting compounds)[24-26]. ***At the low concentration regime, the degradation reaction rate on the catalyst surface scales linearly with the adsorption constant of the reactant***[27,28]. That is, under this condition, molecular binding affinity has significant influence on the reaction kinetics. For example, when [HQ] is small (and the competitor is absent), Eq. S1 reduces to $v_{HQ} = k_{HQ}K_{HQ}[HQ]$, in which the HQ oxidation rate is linearly dependent on K_{HQ}, the HQ adsorption equilibrium constant. The information on the reactant binding affinity, immediately obtainable by COMPEITS, can guide the design of photocatalysts for maximizing pollutant degradation reaction kinetics. In other words, a photocatalyst particle with its size and shape optimized to yield larger overall molecular adsorption ability is expected to exhibit faster reaction kinetics, under realistic, industrially relevant conditions where the pollutant concentration is low, provided that the difference in the catalytic rate constant does not overwhelm the difference in catalytic behaviors.

Moreover, the process of sorption/desorption of small molecules onto solid materials alone (i.e., without intended catalysis applications) is of paramount importance for many applications such as separation processes in chemical and environmental industries[24,29-36], which account for about 10 to 25% of the world's energy consumption[29,31]. COMPEITS is well poised to interrogate these adsorption processes with nanometer spatial resolution under operando conditions. For example, COMPEITS can quantify, at the single-particle or sub-particle level, the molecular binding affinity of an adsorbent material, a key performance metric for adsorbents[37,38]. Such knowledge is challenging to acquire without the use of COMPEITS. Additionally, information of molecular binding affinity of an adsorbent is directly related to selectivity control (i.e., a large difference in binding affinity between two pollutants indicates high selectivity), a long-standing challenge in chemical separation[39]. Hence, because of its ability to provide spatially-resolved, quantitative information on molecular binding, COMPEITS can be used to reveal optimal binding sites, and thus predict the optimal size, or shape, or their combination for an adsorbent material to achieve high separation efficiency, low energy cost, and high molecular selectivity.

In a broader context, the ability of COMPEITS to study molecular adsorption make this technique a potentially powerful tool for advancing materials science and nanotechnology. COMPEITS is suitable for elucidating the molecular binding processes (for various types of adsorbates beyond HQ reported here, e.g., ions, synthetic polymers, proteins, gas molecules) that occur on several material systems of imminent importance, such as graphene-based materials[35,40-43], carbon nanotubes[44,45], nanoparticles[46], metal-organic frameworks[32,36,47-50], covalent organic frameworks[51], etc. Such knowledge, if it were to become available through the use of COMPEITS, would open new avenues for rational design of these materials systems for optimal performance, and would be directly conducive to addressing some important fundamental questions in materials engineering, such as where adsorbates bind preferentially (e.g., edge sites versus basal plane in

two-dimensional materials), how fast they bind, and how the binding location distribution affects the optical, electronic and magnetic properties of these materials.

Furthermore, COMPEITS not only maps the position of molecular binding, but yields quantitative information of the strength of such molecular binding because COMPEITS allows for systematic titration to modulate the degree of competition between the target and auxiliary processes. Moreover, in additional to spatial information, COMPEITS can also offer temporal information of molecular binding, and thus can be used to study transient dynamics of these binding processes. Also, notably, while other microscopy techniques (such as atomic force microscopy[52] and scanning tunneling microscopy[53,54]) have been used to interrogate molecular binding on solid surfaces for unlabeled nonfluorescent small molecules, COMPEITS is the first optical microscopy technique that can do so and enjoys the ease of experimental implementation, especially under ambient, operando, solution conditions.

2.2. Typical ranges for the size and shape parameters of $BiVO_4$ particles of tetragonal bifrustum morphology.

Supplementary Table 5. The typical ranges for the size parameter L and the shape parameter ξ for $BiVO_4$ particles of tetragonal bifrustum morphology

Size parameter L (μm)	Shape parameter ξ	References
2 – 12	0.4 – 0.7	[55]
1 – 3	0.6 – 0.8	[1]
3 – 4	0.7 – 0.8	[56]
1 – 2	0.6 – 0.7	[57]
2 – 5	0.7 – 0.8	[58]
4 – 9	0.6 – 0.7	[59]
1	0.7	[60]
0.7 – 1.2	0.3 – 0.8	[61]
0.8 – 1.5	0.3 – 0.7	[62]
0.8 – 1.5	0.7 – 0.8	[63]
4	0.7	[64]
1 – 1.5	0.3 – 0.6	[65]
1	0.6	[66]
1	0.3 – 0.5	[67]
5	0.6	[68]
10 – 14	0.6 – 0.8	[69]

2.3. Energy-level analysis to show that the photogenerated holes in $BiVO_4$ can oxidize HQ and AR.

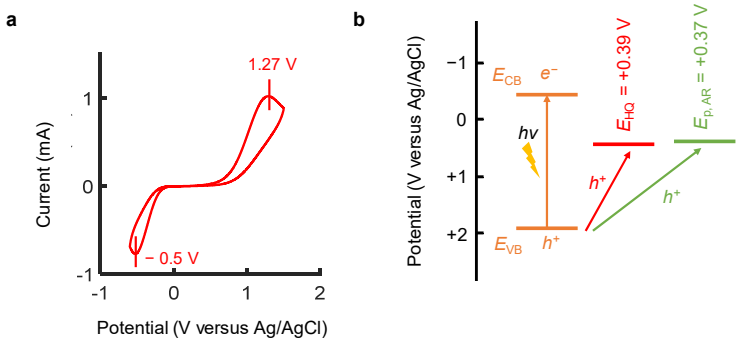

Supplementary Figure 11. Energy-level analysis to show that the photogenerated holes in $BiVO_4$ can oxidize HQ and AR. **a**, Cyclic voltammogram of 10 mM HQ in N_2-purged 0.1 M Na_2SO_4 pH 7.4 0.1 M phosphate buffer. Scan rate: 10 mV/s. The formal potential of the HQ/Q redox couple (E_{HQ}) was determined as the average of the reversible oxidation peak potential (1.27 versus Ag/AgCl) and the reversible reduction peak potential (−0.5 V versus Ag/AgCl). **b**, Energy-level diagram (in reference to Ag/AgCl) of E_{HQ} and the peak oxidation potential of AR ($E_{p,\,AR}$)[11] relative to the conduction band (E_{CB}) and valence band (E_{VB}) edges of $BiVO_4$. *hv* indicates incident light. The red and green arrows illustrate schematically the energetically possible pathways of photogenerated holes in $BiVO_4$ to HQ and AR, respectively.

2.4. Under dark conditions there is no significant AR or HQ oxidation.

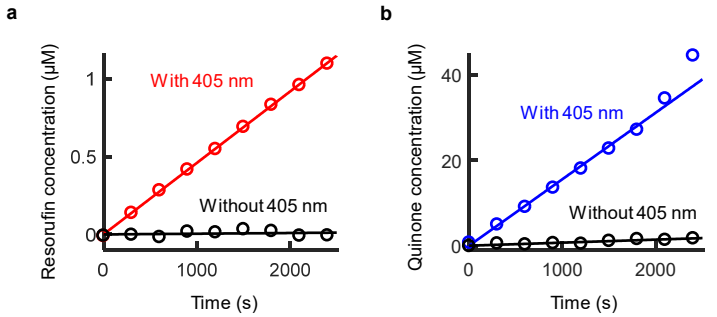

Supplementary Figure 12. Control experiments showing that under dark conditions there is no significant AR or HQ oxidation. Resorufin concentration (**a**) or quinone concentration (**b**) versus time with and without the 405 nm laser illumination using a bulk $BiVO_4$ film as the photoelectrocatalyst on an electrode (applied potential = 0.2 V versus Ag/AgCl; initial concentrations of HQ and AR are 500 and 40 μM, respectively). The concentrations of resorufin and quinone were measured by fluorescence emission spectroscopy and UV-vis absorption spectroscopy, respectively (see the main text Fig. 1c for example). Open symbols: experimental data. Solid lines: linear fits.

2.5. The AR/HQ system follows a competitive inhibition behavior instead of an uncompetitive inhibition behavior.

In the case of a competitive inhibition (i.e., the two reactants compete for the same surface sites), the rate of the product formation in the AR oxidation reaction should be described by Eq. 1 in the main text. If an uncompetitive inhibition behavior were to be assumed (i.e., the two reactants bind to adjacent but different surface sites), this reaction rate should have been described by the following alternative equation [2]:

$$v_{AR} = \frac{k_{AR} K_{AR} [AR]}{1 + K_{AR} [AR](1 + K_{HQ} [HQ])} \qquad \text{Eq. S55}$$

where v_{AR} and k_{AR} are the specific rate and specific rate constant of AR oxidation reaction, K_{AR} and K_{HQ} are the adsorption equilibrium constants for AR and HQ on the catalyst surface, respectively. In order to rule out the possibility of an uncompetitive inhibition behavior in our system, we measured the v_{AR} versus [HQ] at two different fixed AR concentrations (40 and 5 μM). Plotting $1/v_{AR}$ versus [HQ] for the two cases with different AR concentrations would yield different behaviors, depending on whether the AR/HQ system follows competitive inhibition or uncompetitive inhibition. In the case of competitive inhibition, the slope of $1/v_{AR}$ versus [HQ] is $\frac{K_{HQ}}{k_{AR}K_{AR}[AR]}$, which is inversely proportional to [AR]. In the case of uncompetitive inhibition, the slope of $1/v_{AR}$ versus [HQ] is $\frac{K_{HQ}}{k_{AR}}$, which is independent of [AR]. Therefore, if the AR/HQ system follows competitive inhibition, the slopes for the two cases with different AR concentrations should be significantly different, the ratio of the two slopes should be close to the inverse ratio of the two AR concentrations. Alternatively, if the AR/HQ system follows uncompetitive inhibition, the slopes for the two cases with different AR concentrations should be the same. As shown in Supplementary Figure 13, the slope for the case with [AR] = 5 μM is clearly different from that with [AR] = 40 μM, and the ratio between the two slopes (8.82 ± 0.37; error bar represents s.d.) is similar to the inverse ratio of the two AR concentrations (40 / 5 = 8).

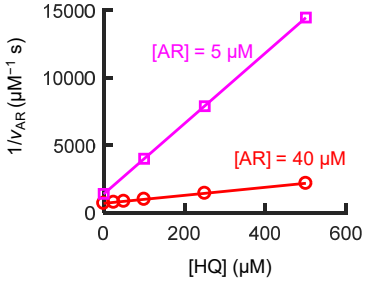

Supplementary Figure 13. $1/v_{AR}$ versus [HQ] with a fixed AR concentration of 5 or 40 μM under photoelectrocatalytic conditions using a bulk $BiVO_4$ film electrode. Open symbols: experimental data. Solid lines: linear fits. The slopes for the cases with [AR] = 5 and 40 μM are 26.1 ± 0.3 and 2.96 ± 0.12 μM^{-2} s (error bars: s.d.), respectively.

2.6. Additional examples of COMPEITS imaging results

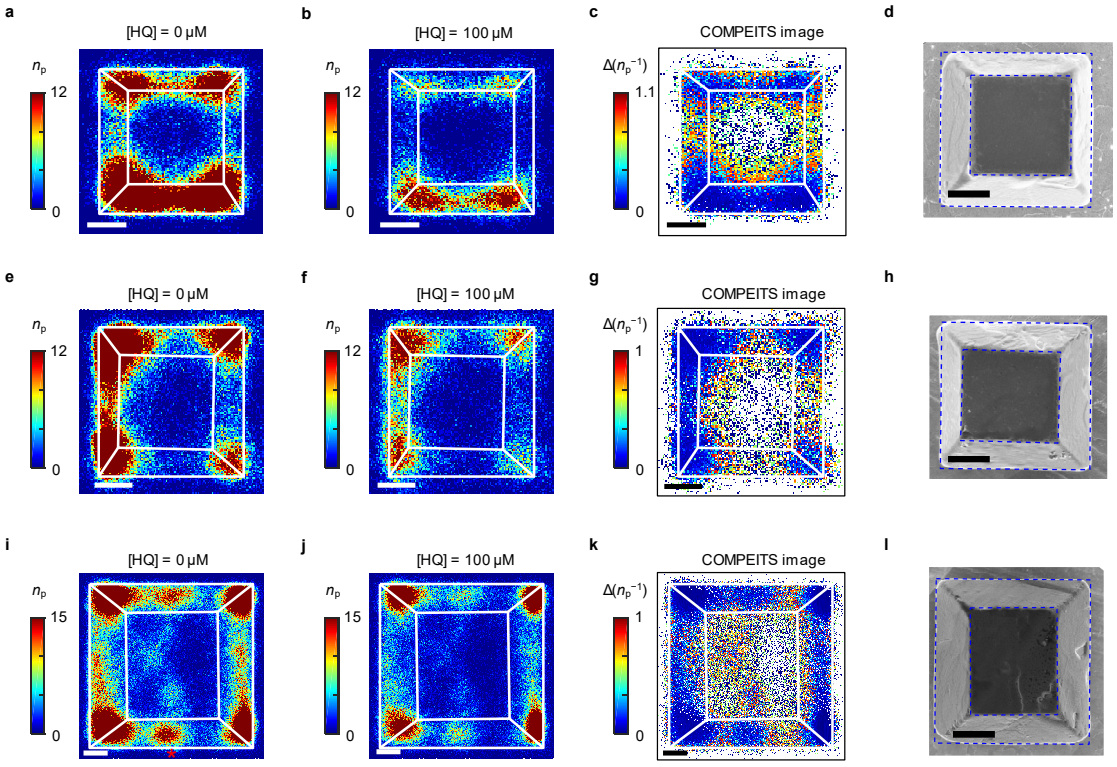

Supplementary Figure 14. Additional examples of COMPEITS imaging results. a-b, Image plot (i.e., two-dimensional histogram) of the number of detected resorufin product molecules, n_p, over a period 22.5 min in the absence (**a**) or presence of 100 μM HQ (**b**). [AR] = 50 nM. Bin size: 35.1^2 nm^2. White line: structural contour determined from the SEM in **d**. **c**, COMPEITS image derived from differences in n_p^{-1} between **b** and **a**. **d**, SEM image of the $BiVO_4$ particle in **a-c** in the same orientation. Dashed line indicates the structural contour that corresponds to the while line in **a-c**. **e-h**, Same as **a-d**, except that Bin size = 33.6^2 nm^2, for a different particle. **i-l**, Same as **a-d**, except that bin size = 31.7^2 nm^2, for another particle. All scale bars: 1 μm.

2.7. Complete data for the HQ titration experiments

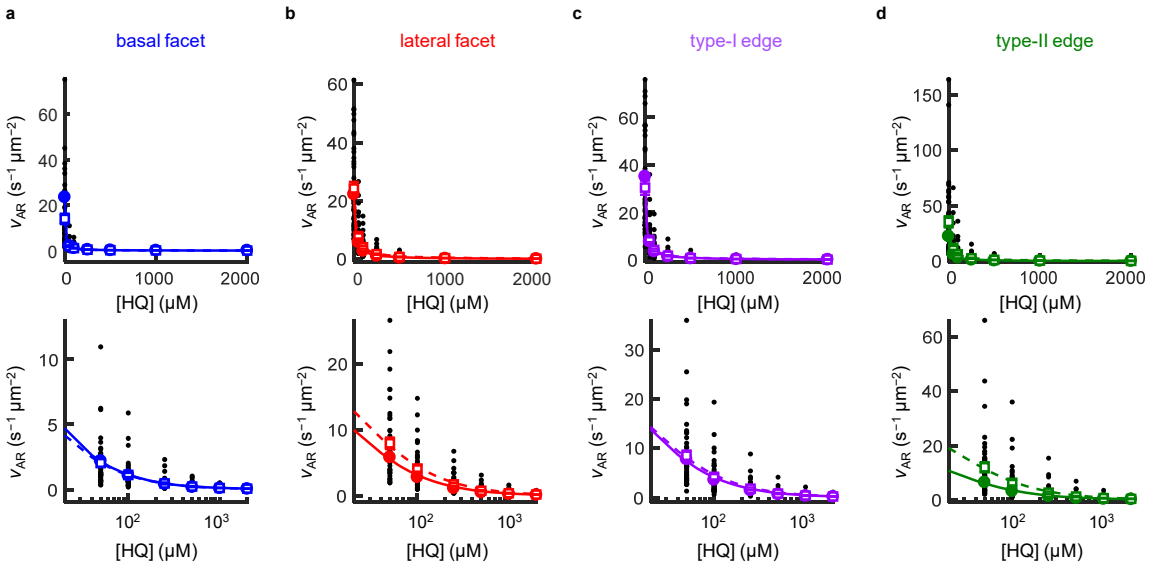

Supplementary Figure 15. The dependence of the specific AR reaction rate, v_{AR}, on the HQ concentration at a fixed AR concentration of 50 nM for the basal {010} facet (**a**), lateral {110} facet (**b**), type-I edge (**c**), and type-II edge (**d**). Solid circles: data from the particle in main text Fig. 2 a-e. Open squares: data averaged over all the 42 particles measured. Black dots: data for all the individual 42 particles. Top panels: linear scale for the horizontal axis. Bottom panels: log scale for the horizontal axis, which does not show the first data point at [HQ] = 0 μM. Error bars: s.e.m. Lines: fits with Eq. 1. The values of the fitting parameters for the ensemble-averaged data (i.e., the dash lines): for the basal {010} facet, k_{AR} = (9.24 ± 0.02) × 10^2 s^{-1} μm^{-2} and K_{HQ} = (1.19 ± 0.01) × 10^{-1} μM^{-1}; for the lateral {110} facet, k_{AR} = (3.10 ± 0.09) × 10^3 s^{-1} μm^{-2} and K_{HQ} = (4.51 ± 0.53) × 10^{-2} μM^{-1}; for the type-I edge, k_{AR} = (3.58 ± 0.10) × 10^3 s^{-1} μm^{-2} and K_{HQ} = (5.62 ± 0.71) × 10^{-2} μM^{-1}; for the type-II edge, k_{AR} = (4.98 ± 0.16) × 10^3 s^{-1} μm^{-2} and K_{HQ} = (4.31 ± 0.58) × 10^{-2} μM^{-1}. (Error bars: s.d.). These K_{HQ} values are in accordance with that obtained from ensemble experiments (i.e., within the same order of magnitude; see Supplementary Note 1.2).

2.8. Modelling the size and shape dependences of $K_{HQ}^{\{010\}}$ and $K_{HQ}^{\{110\}}$

We modeled the measured size and shape dependences of K_{HQ} for each facet type using the following equation:

$$K_{HQ} = \beta_1 \exp\left(\frac{\beta_2}{L}\right)\exp\left(-\beta_3\xi\right) \qquad \text{Eq. S56}$$

where β_i (i = 1, 2, or 3) are positive scaling parameters.

The scaling relation with L (i.e., $\exp\left(\frac{\beta_2}{L}\right)$) is based on a thermodynamic model that uses the size dependence of the particle surface energy to derive that the molecular adsorption free energy scales as $\frac{1}{L}$, where L is the size parameter (i.e., characteristic length scale) of the particle[27,70]. The molecular adsorption equilibrium constant consequently scales as $\exp\left(\frac{1}{L}\right)$ [27,70]. Notably, this size dependence is only applicable to particles containing more than about 100 atoms (or, with L typically >> 10 nm), which corresponds to a size regime whereby the energy level splitting is significantly smaller than the thermal energy and the quantum size effects are negligible[27,70,71]. Therefore, this scaling relation with L is applicable to the 42 particles measured in our study, the size of which ranges from ~3000 to ~7000 nm.

The scaling relation with ξ (i.e., $\exp(-\beta_3\xi)$) is empirically chosen because it can satisfactorily describe the experimentally observed, asymptotic decrease of K_{HQ} with an increasing ξ, and also because it can extrapolate to the two physically meaningful limiting cases (i.e., $\xi = 0$ or 1, corresponding to a perfect bipyramid or a perfect plate).

The values of the fitting parameters are given in Supplementary Table 6. β_1 of the {110} facet corresponds to the K_{HQ} value of an infinitely large bipyramid-shaped particle. $\beta_1 \exp(-\beta_3)$ of the {010} facet corresponds to the K_{HQ} value of an infinitely large plate-shaped particle. β_2 and β_3 describe the steepness of the decaying K_{HQ} versus L and ξ, respectively.

The size scaling parameter β_2 for the basal {010} facet is ~10 times larger than for the lateral {110} facet, quantifying the faster decay of $K_{HQ}^{\{010\}}$ with increasing the particle size L. The shape scaling parameter β_3 for the basal {010} facet is slightly larger, consistent with the steeper decay of $K_{HQ}^{\{010\}}$ when the particle shape transitions from bipyramid-like to plate-like (i.e., with increasing ξ).

Supplementary Table 6. Values of the fitting parameters of the two-dimensional model that describes the size and shape dependences of $K_{HQ}^{\{010\}}$ and $K_{HQ}^{\{110\}}$ (Error bar: s.d.)

	β_1 (μM^{-1})	β_2 (nm)	β_3
{010} basal facet	0.11 ± 0.05	8360 ± 700	3.06 ± 0.66
{110} lateral facet	0.23 ± 0.11	830 ± 620	2.65 ± 0.56

2.9. Other ratios of K_{HQ}

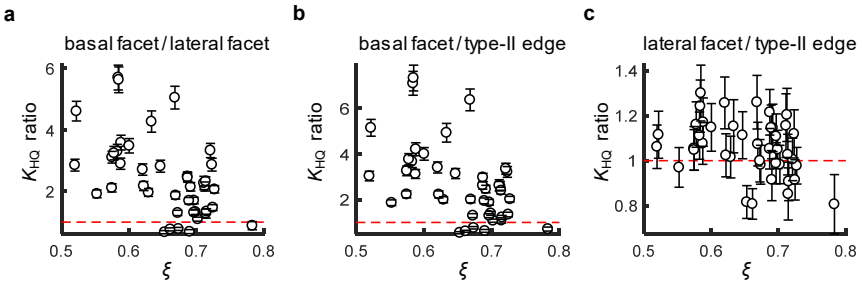

Supplementary Figure 16. Other ratios of K_{HQ} between the type-I edge, the type-II edge, the basal {010} facet, and the lateral {110} facet, as a function of particle shape parameter ξ. Red dashed line marks ratio = 1. Error bars: s.d.

2.10. Calculation of K_{HQ}^{whole} and ω_{HQ}

The fitted parameters for the basal and lateral facets (Supplementary Table 6) can be used to predict the overall HQ adsorption equilibrium constant (K_{HQ}^{whole}) for a whole $BiVO_4$ particle of any physically accessible size and shape (L: ~1-10 μm; ξ: ~0.3-0.8; Supplementary Table 5). Because adsorption equilibrium constant is a per surface-site-based chemical property, K_{HQ}^{whole}, the adsorption equilibrium constant of a whole particle should be the surface-area–weighted average of its composing facets, and is calculated as $K_{HQ}^{whole} = \frac{K_{HQ}^{\{010\}}A^{\{010\}} + K_{HQ}^{\{110\}}A^{\{110\}}}{A}$, where $K_{HQ}^{\{010\}}$ and $K_{HQ}^{\{110\}}$ can be directly determined from the fitted parameters for the basal and lateral facets for any given (L, ξ), and $A^{\{010\}}$, $A^{\{110\}}$, and A are the surface area of the {010} basal facet, the surface area of the {110} facet, and the total surface area of a whole particle, all of which can be determined for any given (L, ξ) (Supplementary Table 7). Please note

that this calculation of K_{HQ}^{whole} implicitly includes the contribution of all edges, as the edge regions are part of the facets as we defined in Figs. 2 f and g.

Moreover, the particle's overall capability of adsorbing HQ reflecting the per unit-mass level, ω_{HQ}, can be directly calculated as $K_{HQ}^{whole}\frac{A}{V}$, where V is the total volume of a whole particle, and can be quantified for any given (L, ξ) (Supplementary Table 7).

Supplementary Table 7. Calculation of the surface area of each type of facet, and the total surface area and volume of a whole particle from the size and shape parameters (i.e., L and ξ).

Description	Symbol	Formula
Surface area of the {010} basal facet	$A^{\{010\}}$	$2\xi^2L^2$
Surface area of the {110} lateral facet	$A^{\{110\}}$	$2\sqrt{2}L^2\left(1-\xi^2\right)$
Total surface area of a whole $BiVO_4$ particle	A	$2\xi^2L^2+2\sqrt{2}L^2\left(1-\xi^2\right)$
Total volume of a whole $BiVO_4$ particle	V	$1/3L^3\left(1-\xi^3\right)$

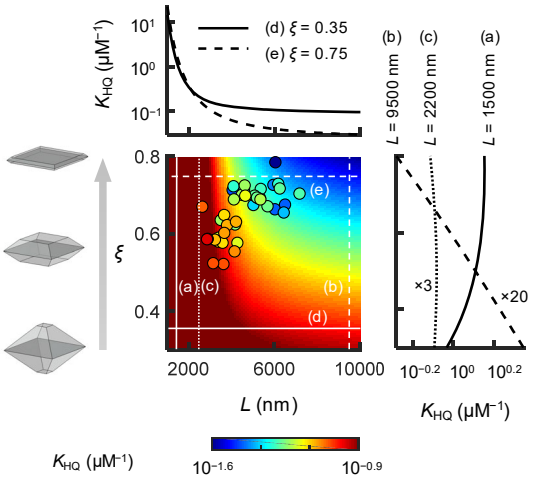

Supplementary Figure 17. Size- and shape-dependences of K_{HQ}^{whole}. Bottom left: two-dimensional dependences of K_{HQ}^{whole} on L and ξ. Solid circles: experimental data determined from HQ titration curves at the whole-particle level (see Supplementary Figure 18). Each solid circle represents one particle; total 42 particles. Shaded surface: predicted values using the fitted parameters of dissected facets (Supplementary Table 6). Top: L dependence of K_{HQ}^{whole} at selected ξ values. Right: ξ dependence of K_{HQ}^{whole} at selected L values.

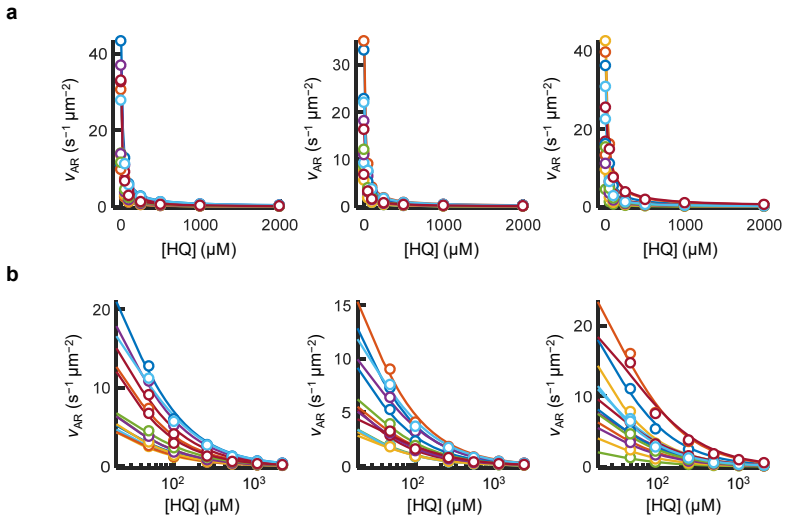

Supplementary Figure 18. The dependence of the specific AR reaction rate, v_{AR}, quantified at the whole-particle level, on the HQ concentration at a fixed AR concentration of 50 nM, with a linear scale (**a**) or a log scale (**b**) for the horizontal axis. Note that for the log scale the data at [HQ] = 0 μM are not visible. Open symbols: experimental data. Lines: fits with Eq. 1. Each of three panels in A or B contains data for 14 different particles, and thus A or B show data from all the 42 particles.

2.11. Comparison of the photophysics of the probe molecule (i.e., the product molecule from AR oxidation) before and after introducing HQ

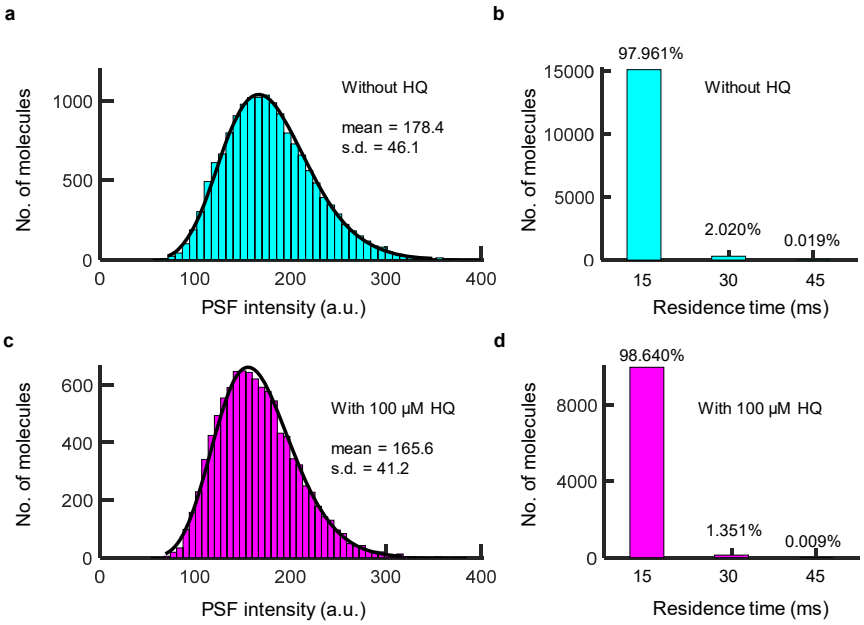

Supplementary Figure 19. Comparison of photophysics of the product molecule resorufin before and after introduction of HQ. a, Distribution of the integrated point-spread-function (PSF) intensity of single-molecule events (i.e., signals from single resorufin molecules) without introduction of HQ. Black solid line: fit with a Gamma distribution. **b**, Distribution of the residence time of resorufin molecules without introduction of HQ. Our imaging experiments were performed with a 15 ms frame rate, so most of the detected single-molecule events lasted for about 1 frame (i.e., 15 ms). **c**, same as **a** except in the presence of 100 μM

HQ. **d**, same as **b** except in the presence of 100 μM HQ. By comparing **a**-**b** with **c**-**d**, it can be seen that before and after introducing HQ, there is no significant difference in the PSF intensity and residence time of the probe molecule (i.e., resorufin).

3. Additional references

1 Li, R. G. *et al.* Spatial separation of photogenerated electrons and holes among {010} and {110} crystal facets of $BiVO_4$. *Nat Commun* **4**, 1432 (2013).

2 Voet, D., Voet, J. G. & Pratt, C. W. *Fundamentals of biochemistry: Life at the molecular level*. 4th edn, (Wiley, 2013).

3 Tachikawa, T., Yonezawa, T. & Majima, T. Super-resolution mapping of reactive sites on titania-based nanoparticles with water-soluble fluorogenic probes. *ACS Nano* **7**, 263-275 (2013).

4 Hodgson, G. K., Impellizzeri, S. & Scaiano, J. C. Dye synthesis in the pechmann reaction: Catalytic behaviour of samarium oxide nanoparticles studied using single molecule fluorescence microscopy. *Chem Sci* **7**, 1314-1321 (2016).

5 Ristanovic, Z., Kubarev, A. V., Hofkens, J., Roeffaers, M. B. J. & Weckhuysen, B. M. Single molecule nanospectroscopy visualizes proton-transfer processes within a zeolite crystal. *J Am Chem Soc* **138**, 13586-13596 (2016).

6 Chen, P. *et al.* Spatiotemporal catalytic dynamics within single nanocatalysts revealed by single-molecule microscopy. *Chem Soc Rev* **43**, 1107-1117 (2014).

7 Zhang, Y. W. *et al.* Superresolution fluorescence mapping of single-nanoparticle catalysts reveals spatiotemporal variations in surface reactivity. *Proc Natl Acad Sci USA* **112**, 8959-8964 (2015).

8 Chen, T. *et al.* Optical super-resolution imaging of surface reactions. *Chem Rev* **117**, 7510-7537 (2017).

9 Ng, J. D. *et al.* Single-molecule investigation of initiation dynamics of an organometallic catalyst. *J Am Chem Soc* **138**, 3876-3883 (2016).

10 Chen, T. Y. *et al.* Concentration- and chromosome-organization-dependent regulator unbinding from DNA for transcription regulation in living cells. *Nat Commun* **6**, 7445 (2015).

11 Sambur, J. B. *et al.* Sub-particle reaction and photocurrent mapping to optimize catalyst-modified photoanodes. *Nature* **530**, 77-80 (2016).

12 Park, Y., McDonald, K. J. & Choi, K. S. Progress in bismuth vanadate photoanodes for use in solar water oxidation. *Chem Soc Rev* **42**, 2321-2337 (2013).

13 Cendula, P. *et al.* Calculation of the energy band diagram of a photoelectrochemical water splitting cell. *J Phys Chem C* **118**, 29599-29607 (2014).

14 Tan, M. X. *et al.* in *Prog inorg chem* 21-144 (John Wiley & Sons, Inc., 2007).

15 Ma, Y., Pendlebury, S. R., Reynal, A., Le Formal, F. & Durrant, J. R. Dynamics of photogenerated holes in undoped $BiVO_4$ photoanodes for solar water oxidation. *Chem Sci* **5**, 2964-2973 (2014).

16 Cooper, J. K. *et al.* Electronic structure of monoclinic $BiVO_4$. *Chem Mater* **26**, 5365-5373 (2014).

17 Sivula, K. & van de Krol, R. Semiconducting materials for photoelectrochemical energy conversion. *Nat Rev Mater* **1**, 15010 (2016).

18 Abdi, F. F., Savenije, T. J., May, M. M., Dam, B. & van de Krol, R. The origin of slow carrier transport in $BiVO_4$ thin film photoanodes: A time-resolved microwave conductivity study. *J Phys Chem Lett* **4**, 2752-2757 (2013).

19 Buxbaum, G. *Industrial inorganic pigments*. 2nd completely rev. edn, (Wiley-VCH, 1998).

20 Mo, G. C. H. *et al.* Genetically encoded biosensors for visualizing live-cell biochemical activity at super-resolution. *Nat Methods* **14**, 427-434 (2017).

21 Folling, J. *et al.* Fluorescence nanoscopy by ground-state depletion and single-molecule return. *Nat Methods* **5**, 943-945 (2008).

22 Huang, H., Dorn, A., Nair, G. P., Bulovic, V. & Bawendi, M. G. Bias-induced photoluminescence quenching of single colloidal quantum dots embedded in organic semiconductors. *Nano Lett* **7**, 3781-3786 (2007).
23 Oishi, M., Tamura, A., Nakamura, T. & Nagasaki, Y. A smart nanoprobe based on fluorescence-quenching pegylated nanogels containing gold nanoparticles for monitoring the response to cancer therapy. *Adv Funct Mater* **19**, 827-834 (2009).
24 Alsbaiee, A. *et al.* Rapid removal of organic micropollutants from water by a porous beta-cyclodextrin polymer. *Nature* **529**, 190-U146 (2016).
25 Schwarzenbach, R. P. *et al.* The challenge of micropollutants in aquatic systems. *Science* **313**, 1072-1077 (2006).
26 Shannon, M. A. *et al.* Science and technology for water purification in the coming decades. *Nature* **452**, 301-310 (2008).
27 Zhou, X. C., Xu, W. L., Liu, G. K., Panda, D. & Chen, P. Size-dependent catalytic activity and dynamics of gold nanoparticles at the single-molecule level. *J Am Chem Soc* **132**, 138-146 (2010).
28 Zhou, X. C. *et al.* Quantitative super-resolution imaging uncovers reactivity patterns on single nanocatalysts. *Nat Nanotechnol* **7**, 237-241 (2012).
29 Sholl, D. S. & Lively, R. P. Seven chemical separations to change the world. *Nature* **532**, 435-437 (2016).
30 Suss, M. E. *et al.* Water desalination via capacitive deionization: What is it and what can we expect from it? *Energy & Environmental Science* **8**, 2296-2319 (2015).
31 Mao, X. *et al.* Energetically efficient electrochemically tunable affinity separation using multicomponent polymeric nanostructures for water treatment. *Energy & Environmental Science*2018).
32 Cadiau, A. *et al.* Hydrolytically stable fluorinated metal-organic frameworks for energy-efficient dehydration. *Science* **356**, 731-735 (2017).
33 Behl, M., Yeom, J., Lineberry, Q., Jain, P. K. & Shannon, M. A. A regenerable oxide-based H_2S adsorbent with nanofibrous morphology. *Nat Nanotechnol* **7**, 810-815 (2012).
34 Ren, Y. *et al.* Superhydrophobic, surfactant-doped, conducting polymers for electrochemically reversible adsorption of organic contaminants. *Advanced Functional Materials* **28**, 1801466 (2018).
35 Chen, L. *et al.* Ion sieving in graphene oxide membranes via cationic control of interlayer spacing. *Nature* **550**, 380-383 (2017).
36 Sung Cho, H. *et al.* Extra adsorption and adsorbate superlattice formation in metal-organic frameworks. *Nature* **527**, 503-507 (2015).
37 Abney, C. W., Gilhula, J. C., Lu, K. & Lin, W. Metal-organic framework templated inorganic sorbents for rapid and efficient extraction of heavy metals. *Adv Mater* **26**, 7993-7997 (2014).
38 Alvarez, P. J. J., Chan, C. K., Elimelech, M., Halas, N. J. & Villagran, D. Emerging opportunities for nanotechnology to enhance water security. *Nat Nanotechnol* **13**, 634-641 (2018).
39 Su, X. *et al.* Asymmetric faradaic systems for selective electrochemical separations. *Energy & Environmental Science* **10**, 1272-1283 (2017).
40 Qin, W., Li, X., Bian, W. W., Fan, X. J. & Qi, J. Y. Density functional theory calculations and molecular dynamics simulations of the adsorption of biomolecules on graphene surfaces. *Biomaterials* **31**, 1007-1016 (2010).
41 Shi, G. *et al.* Two-dimensional NaCl crystals of unconventional stoichiometries on graphene surface from dilute solution at ambient conditions. *Nat Chem* **10**, 776-779 (2018).
42 Katoch, J. *et al.* Structure of a peptide adsorbed on graphene and graphite. *Nano Lett* **12**, 2342-2346 (2012).
43 Kim, S. N. *et al.* Preferential binding of peptides to graphene edges and planes. *J Am Chem Soc* **133**, 14480-14483 (2011).

44 Zhang, J. *et al.* Molecular recognition using corona phase complexes made of synthetic polymers adsorbed on carbon nanotubes. *Nat Nanotechnol* **8**, 959-968 (2013).

45 Landry, M. P. *et al.* Single-molecule detection of protein efflux from microorganisms using fluorescent single-walled carbon nanotube sensor arrays. *Nat Nanotechnol* **12**, 368-377 (2017).

46 Cedervall, T. *et al.* Understanding the nanoparticle-protein corona using methods to quantify exchange rates and affinities of proteins for nanoparticles. *Proc Natl Acad Sci U S A* **104**, 2050-2055 (2007).

47 Jawahery, S. *et al.* Adsorbate-induced lattice deformation in IRMOF-74 series. *Nat Commun* **8**, 13945 (2017).

48 McDonald, T. M. *et al.* Cooperative insertion of CO_2 in diamine-appended metal-organic frameworks. *Nature* **519**, 303-308 (2015).

49 Lee, K., Howe, J. D., Lin, L.-C., Smit, B. & Neaton, J. B. Small-molecule adsorption in open-site metal–organic frameworks: A systematic density functional theory study for rational design. *Chemistry of Materials* **27**, 668-678 (2015).

50 Kubota, R., Tashiro, S., Shiro, M. & Shionoya, M. In situ X-ray snapshot analysis of transient molecular adsorption in a crystalline channel. *Nat Chem* **6**, 913-918 (2014).

51 Li, J. *et al.* $^{99}TcO_4^-$ remediation by a cationic polymeric network. *Nat Commun* **9**, 3007 (2018).

52 Gross, L., Mohn, F., Moll, N., Liljeroth, P. & Meyer, G. The chemical structure of a molecule resolved by atomic force microscopy. *Science* **325**, 1110-1114 (2009).

53 Li, S. C., Chu, L. N., Gong, X. Q. & Diebold, U. Hydrogen bonding controls the dynamics of catechol adsorbed on a TiO_2(110) surface. *Science* **328**, 882-884 (2010).

54 Bikondoa, O. *et al.* Direct visualization of defect-mediated dissociation of water on TiO_2(110). *Nat Mater* **5**, 189 (2006).

55 Wang, D. *et al.* Crystal facet dependence of water oxidation on bivo4 sheets under visible light irradiation. *Chem–Eur J* **17**, 1275-1282 (2011).

56 Li, H., Yu, H., Quan, X., Chen, S. & Zhao, H. Improved photocatalytic performance of heterojunction by controlling the contact facet: High electron transfer capacity between TiO_2(110) and the {110} facet of $BiVO_4$ caused by suitable energy band alignment. *Advanced Functional Materials* **25**, 3074-3080 (2015).

57 Li, R., Han, H., Zhang, F., Wang, D. & Li, C. Highly efficient photocatalysts constructed by rational assembly of dual-cocatalysts separately on different facets of $BiVO_4$. *Energ Environ Sci* **7**, 1369-1376 (2014).

58 Kim, Y. *et al.* Hybrid z-scheme using photosystem I and $BiVO_4$ for hydrogen production. *Advanced Functional Materials* **25**, 2369-2377 (2015).

59 Zhu, J. *et al.* Direct imaging of highly anisotropic photogenerated charge separations on different facets of a single $BiVO_4$ photocatalyst. *Angew Chem Int Ed Engl* **54**, 9111-9114 (2015).

60 Tachikawa, T., Ochi, T. & Kobori, Y. Crystal-face-dependent charge dynamics on a $BiVO_4$ photocatalyst revealed by single-particle spectroelectrochemistry. *ACS Catal* **6**, 2250-2256 (2016).

61 Tan, H. L., Wen, X., Amal, R. & Ng, Y. H. Bivo4 {010} and {110} relative exposure extent: Governing factor of surface charge population and photocatalytic activity. *J Phys Chem Lett* **7**, 1400-1405 (2016).

62 Tan, H. L. *et al.* Interfacing $BiVO_4$ with reduced graphene oxide for enhanced photoactivity: A tale of facet dependence of electron shuttling. *Small* **12**, 5295-5302 (2016).

63 Wang, T. *et al.* Reduced graphene oxide (RGO)/$BiVO_4$ composites with maximized interfacial coupling for visible lght photocatalysis. *ACS Sustain Chem Eng* **2**, 2253-2258 (2014).

64 Feng, W., Weng, S., Zheng, Z., Fang, Z. & Liu, P. Rational design of a charge shunt: Modification upon crystal facet engineering of semiconductor photocatalysts. *Chem Commun (Camb)* **51**, 11186-11189 (2015).

65 Tan, H. L. *et al.* Enhancing the photoactivity of faceted $BiVO_4$ via annealing in oxygen-deficient condition. *Particle & Particle Systems Characterization* **34**, 1600290 (2017).

66 Tan, H. L., Amal, R. & Ng, Y. H. Exploring the different roles of particle size in photoelectrochemical and photocatalytic water oxidation on $BiVO_4$. *ACS Appl Mater Inter* **8**, 28607-28614 (2016).
67 Sun, J., Chen, G., Wu, J., Dong, H. & Xiong, G. Bismuth vanadate hollow spheres: Bubble template synthesis and enhanced photocatalytic properties for photodegradation. *Appl Catal B-Environ* **132-133**, 304-314 (2013).
68 Melo, M. A., Jr. *et al.* Surface photovoltage measurements on a particle tandem photocatalyst for overall water splitting. *Nano Lett* **18**, 805-810 (2018).
69 Zhu, J. *et al.* Visualizing the nano cocatalyst aligned electric fields on single photocatalyst particles. *Nano Lett* **17**, 6735-6741 (2017).
70 Parmon, V. N. Thermodynamic analysis of the effect of the nanoparticle size of the active component on the adsorption equilibrium and the rate of heterogeneous catalytic processes. *Dokl Phys Chem* **413**, 42-48 (2007).
71 Yudanov, I. V., Genest, A., Schauermann, S., Freund, H. J. & Rosch, N. Size dependence of the adsorption energy of CO on metal nanoparticles: A DFT search for the minimum value. *Nano Lett* **12**, 2134-2139 (2012).